ÉCOLE DE TECHNOLOGIE SUPÉRIEURE
UNIVERSITÉ DU QUÉBEC

THESIS PRESENTED TO
ÉCOLE DE TECHNOLOGIE SUPÉRIEURE

IN PARTIAL FULFILLMENT OF THE REQUIREMENTS FOR
A MASTER'S DEGREE WITH THESIS IN AEROSPACE ENGINEERING
M.A.Sc.

BY
Christophe TRAVAGLINI

SIMULATION OF LAMB WAVE PROPAGATION AND INTERACTION WITH DEFECTS USING COMMERCIALLY AVAILABLE SOFTWARE

MONTREAL, DECEMBER 10, 2015

BOARD OF EXAMINERS

THIS THESIS HAS BEEN EVALUATED

BY THE FOLLOWING BOARD OF EXAMINERS:

M. Pierre Bélanger, thesis director
Department of mechanical engineering at École de technologie supérieure

M. Martin Viens, co-advisor
Department of mechanical engineering at École de technologie supérieure

M. Vincent Demers, committee president
Department of mechanical engineering at École de technologie supérieure

M. Olivier Doutres, external examiner
Department of mechanical engineering at École de technologie supérieure

THIS THESIS WAS PRESENTED AND DEFENDED

IN THE PRESENCE OF A BOARD OF EXAMINERS AND THE PUBLIC

ON DECEMBER 8, 2015

AT ÉCOLE DE TECHNOLOGIE SUPÉRIEURE

ACKNOWLEDGEMENTS

First, I would like to thank my research advisors, Pr. Pierre Bélanger and Pr. Martin Viens. They shared their knowledge and their experience, guiding and helping me throughout my dissertation.

I am also thankful to Guillaume Boivin for the time spent on solving our simulation problems, and to Dr. Demartonne Ramos França for his helpful advice along the way.

In addition, I am grateful for the work of Dr. Christophe Bescond on experiments at the National Research Council Canada (NRC). It was greatly appreciated.

This project was rendered possible with the collaboration of École de Technologie Supérieure, Bombardier Aerospace, L3-MAS, Sherbrooke University, the NRC, the Centre Technologique en Aerospatiale (CTA) and McGill University. I express my gratitude to them.

I would also like to acknowledge the Consortium for Research and Innovation in Aerospace in Québec (CRIAQ) as well as NSERC RDC program for its financial support.

SIMULATION DE LA PROPAGATION DES ONDES DE LAMB ET DE LEURS INTÉRACTIONS AVEC DES DÉFAUTS EN UTILISANT DES LOGICIELS COMMERCIAUX

Christophe TRAVAGLINI

RÉSUMÉ

La surveillance de l'integrité structurale consiste en un processus de detection de dommages en continu dans une structure d'ingénierie en utilisant des transducteurs intégrés et les prises de décision résultantes pour la sauvegarder. Un tel système est performant s'il a une bonne sensibilité aux défauts tout en limitant la densité des transducteurs.

Les ondes guidées ultrasonores peuvent se propager sur de longues distances avec une atténuation minimale, cela les rend particulièrement attrayantes pour le contrôle de l'intégrité structurale. Communément, les défauts sont détectés et localisés en soustrayant un signal de base au signal de contrôle.

Les ondes guidées ultrasonores basses fréquences pour les systèmes de surveillance de l'intégrité structurale et les interactions entre les modes de Lamb fondamentaux et des défauts sont des sujets bien documentés dans la littérature scientifique. Cependant il y a un nombre limité d'études sur les modes d'ordres élevés ou à hautes fréquences. Ils pourraient permettre l'abaissement de la limite de détection des systèmes de surveillance structurale par rapport aux systèmes à basses fréquences. Cependant à hautes fréquences, plusieurs modes se propagent et se superposent, ce phénomène et l'atténuation constituent les principales difficultés rencontrées avec ces ondes guidées.

Cette étude examine les avantages des ondes guidées hautes fréquences par rapport aux basses fréquences afin de développer un système de surveillance de l'état des structures à haute sensibilité. La structure étudiée est une plaque d'aluminium de dimensions 305 mmx 305 mm x 1.6 mm avec un trou en son centre.

La structure étudiée a été modélisée par éléments finis pour déterminer le champ d'ondes réémises par une fissure sur la circonférence du trou. L'effet de la fissure sur les signaux est étudié par la variation de paramètres tels que son orientation, sa longueur et sa profondeur. Une partie des simulations a été validée par des expériences. Le protocole expérimental comprenait un transducteur piézoélectrique collé sur la tranche de la plaque et un vibromètre laser pour la détection. Des excitations à 100kHz et à 4MHz ont été utilisées pour les basses et hautes fréquences respectivement.

Mots clés: Ultrasons, ondes guidées, intégrité structurale, hautes fréquences

SIMULATION OF LAMB WAVE PROPAGATION AND INTERACTION WITH DEFECTS USING COMMERCIALLY AVAILABLE SOFTWARE

Christophe TRAVAGLINI

ABSTRACT

Structural Health Monitoring (SHM) consists of the continuous process of damage detection in an engineering component using built-in transducers and any resultant intervention to preserve structural integrity. It is a multidisciplinary field in terms of the technology involved as well as the diverse applications. Good SHM systems are considered those that combine a high sensitivity to defects and a low density of sensors.

Ultrasonic guided waves have the ability to propagate long distances with minimal attenuation making them particularly interesting in SHM applications. Using the baseline subtraction approach, the signal from a defect free structure is compared to the actual monitoring signal in order to detect and characterize defects.

There are many scientific publications on low frequency guided waves for SHM purposes and the interaction between guided wave fundamental modes and defects is also well documented. There are, however, a very limited number of studies on high order modes. High frequency guided waves may enable the detection of smaller cracks relative to conventional low frequency guided waves systems. The main difficulty at high frequency is the co-existence of several modes with different velocities.

This study investigates the advantages of high frequency guided waves relative to low frequency to detect cracks at their initiation. Thus the scattering around a through-thickness hole is studied with a view to develop a highly sensitive SHM method.

2D and 3D finite element models of a 305 mm $\times$ 305 mm $\times$ 1.6 mm aluminum plate were used to determine the scattering of cracks on the circumference of a through-thickness hole in the middle of the plate. Crack properties such as orientation, length and depth were studied in order to characterize the crack using the received signals. A subset of the finite element simulations was validated against experimental results. The experimental setup comprised a classic contact piezoelectric transducer bonded on the side of the plate and a laser Doppler vibrometer for the detection. Input signals centered at 100 kHz and 4 MHz were used in simulations and experiments for low and high frequency studies respectively.

Keywords: Ultrasonic wave, guided wave, structural health monitoring, high frequency

TABLE OF CONTENTS

LIST OF TABLES

LIST OF FIGURES

LIST OF ABREVIATIONS

2D	Two-Dimensions
3D	Three-Dimensions
ALID	Absorbing Layer with Increasing Damping
CFL	Courant-Friedrichs-Lewy
FE	Finite Element
FFT	Fast Fourier Transform
NDT	Non Destructive Testing
NRC	National Research Council Canada
P	Pressure
PML	Perfectly Matched Layer
SH	Shear-Horizontal
SHM	Structural Health Monitoring
SV	Shear-Vertical

LISTE OF SYMBOLS AND UNITS OF MEASUREMENTS

dB	Decibel
g	Gram
Hz	Hertz
m	Meter
Pa	Pascal
s	Second
$\frac{\delta}{\delta}$	Partial derivative
sin	Sinus function
cos	Cosinus function
tan	Tangent function
A_i	Antisymmetric mode of order i
b	Half thickness of the infinite plate used for guided wave definition
$\boldsymbol{C}$	Structural damping matrix
c_g	Group velocity
c_{ph}	Phase velocity
c_L	Longitudinal velocity
c_S	Shear wave velocity
d	Thickness of the infinite plate used for guided wave definition

$\boldsymbol{F}_a$	External loads vector
f	Frequency
$\boldsymbol{K}$	Structural stiffness matrix
k	Wavenumber
k_z	Wavenumber corresponding to a wave propagating along $\boldsymbol{e}_z$ direction
L	Wavelength
$\boldsymbol{M}$	Structural matrix
S_i	Symmetric mode of order i
λ	First Lamé coefficient
μ	Second Lamé coefficient
ν	Poisson coefficient
ρ	Density
ω	Angular frequency

INTRODUCTION

The field of Non Destructive Testing (NDT) is in constant development. It includes a variety of different methods; for example: eddy current, liquid penetrant, radiographic, thermographic, or ultrasonic testing, as presented by Shull (2002). The NDT method objective is the improvement of the reliability and safety of industrial components by monitoring their integrity. In addition, an efficient NDT system enables a reduction of maintenance costs. For these reasons, the development of this domain is crucial for industries such as civil engineering, oil and gas, transport and aerospace.

Using ultrasonic guided waves for NDT is very attractive because of their capability to propagate over long distances with low attenuation. This enables a large area of structures to be tested from a single transducer position. Using guided waves also avoids a point-by-point scanning inspection which is necessary with traditional techniques. Another important advantage is the possibility to inspect inaccessible parts of the structure. There are, however, an infinite number of guided wave modes in structures such as plates, pipes or rails. The acoustic properties of ultrasonic guided waves depend on the structure, the material and the frequency, which means that post-processing is complex when several modes are superposed. However there are currently commercialized systems for pipes and rails testing (Cawley *et al.* (2003); Wilcox *et al.* (2003)) achieved by using deployable arrays of transducers generating and receiving guided waves.

Guided wave Structural Health Monitoring systems (SHM) consist of permanently attached transducers that inspect the structures continuously or on-demand. One system in particular has been commercialized by the company Guided Ultrasonic Ltd.; it is designed to monitor pipes and is called G-PIMS (Cawley *et al.* (2012)).

In order to implement a SHM system for the inspection of a 2D structure (for example a plate), a strategy is necessary to position the transducers and a robust post-processing method is required to detect and identify the defects. This is necessary for every desired case of SHM application regarding the defect type and the monitored structure.

However, the studies achieved to date mainly developed the use of fundamental guided wave modes. Even the studies done at a high frequency–where fundamental modes coexist with higher order modes–only investigated the fundamental modes to inspect the structure.

This work studies the potential of high order modes for detection and monitoring of a crack on the circumference of a through-thickness hole. In the course of this Master's thesis, the finite element simulations are compared to theory and experiments using the mode directivity diagrams in order to validate the models. The simulations are then used to study crack parameters, like length, orientation and depth; and to determine a method to define the crack (in terms of the parameters studied) with an SHM approach.

The objective of this study is to determine if there is an advantage in using high frequency compared to low frequency guided waves, or in using high order modes compared to fundamental modes. Ultimately, the goal is to determine if crack sizing is possible with high order modes in a SHM vision.

In the first chapter, theoretical bases are presented to provide background necessary for an informed understanding of this work. In chapter two, the building of the finite element models is detailed, and the different steps and the influence of each parameter are explained. In the third chapter, the low frequency potential for detection and identification of a crack on a hole circumference is investigated using only the propagation of fundamental modes. Finally, chapter four is a study of the high frequency potential modes up to the third order.

CHAPTER 1

LITERATURE REVIEW

1.1 Structural Health Monitoring

A system that can continuously monitor the integrity of a structure with regard to the presence and growth of defects ideally below critical size is crucial for structure reliability. This type of system is often grouped into the so-called SHM systems. SHM systems are of interest because they may result in significant reductions in maintenance costs by avoiding time-consuming human inspection and programming for replacements of damaged parts. The amount of work on SHM systems has been growing recently in the aerospace, oil and gas, nuclear and civil engineering industries.

An important part of SHM systems is the transducers. Transducers are usually permanently attached to the structure and strategically positioned to achieve the most sensitive detection. The density of transducers has an influence on the sensitivity of the detection as defined by Croxford *et al.* (2007). A compromise must be found between the system sensitivity and the number of sensors, as the number of transducers affects the cost and weight of the system. Moreover complexity increases with transducer density. In addition, a challenge in the implementation of SHM systems is the life of the transducers which must survive harsh environmental conditions and have a life cycle at least as long as the structure on which they are installed.

Defects are detected by the measurement of a given property of the monitored signal and the changes in it over time. Many SHM techniques exist and some are currently being considered, including the vibration-based method by Deraemaeker *et al.* (2008), the impedance-based method by Park and Inman (2005), the ultrasound-based method by Cawley *et al.* (2012) and the fibre optic method by Glisic and Inaudi (2007).

SHM techniques can be classified as active or passive. The active methods excite the structure with an input and analyze its response: for example, the Lamb wave detection by Staszewski *et al.* (2004). Alternatively, the passive methods detect changes in a chosen property of the structure, e.g., the vibration monitoring by Farrar *et al.* (2001).

In the following section, the low frequency methods, acoustic emission and guided wave SHM systems are presented, followed by a review of high frequency work in SHM.

1.1.1 Low frequency ultrasonic waves

1.1.1.1 Acoustic Emission (AE) SHM

Acoustic emission relies on transient sound waves propagating within the structure under analysis. These elastic waves are released when the material is deformed, like when there is a crack (Roberts and Talebzadeh (2003)), or corrosion (Mazille *et al.* (1995)), or delamination in composite (Benmedakhene *et al.* (1999)). The acoustic emission method is attractive because it can monitor structures with very limited access and cover long distances. It has already been investigated for aircraft structures, for example to monitor events during a pressure testing of aircrafts by Dalton *et al.* (2001).

An AE system consists of an array of sensors. When an event occurs in the structure, a number of the sensors will detect it. The system then flags it if its amplitude is above a predetermined threshold. Once the signal is recorded, it is processed to give information about the defect. The post-processing can take a multitude of parameters into account such as the maximum amplitude, the energy, the number of times a given burst crosses the threshold, or the decay time, among others, in order to give information about the location and the identity of the source.

The main problem with acoustic emission is the determination of the threshold, because the source of the emission is often a non-repeatable event and to ensure its recording, the threshold level must be low. A low threshold level increases the probability of false calls due to noise which cannot be reduced by averaging due to the non-repeatable events. The noise level is also known to be high in most industrial applications.

The elastic waves generated by an event in the structure propagate as ultrasonic guided waves. Dalton *et al.* (2001) simulated acoustic emission signals by breaking pencil leads on the surface and on the edge of an aluminum plate (simulating crack growth). It appeared that the fundamental antisymmetric mode A_0 and the symmetric S_0 were predominant when the lead was broken on the surface and the edge respectively. This work also evaluated the frequencies in which the energy was concentrated. For both modes, the peak of energy in the signal was at 65 - 70 kHz with significant energy up to 600 kHz for S_0 and up to 100 kHz for A_0.

1.1.1.2 Ultrasonic Guided wave SHM

At low frequency, ultrasonic guided wave monitoring consists of the generation of fundamental Lamb modes. These waves are attractive because of their long propagation distance and low attenuation. In addition, an SHM system being by nature an active system, the excitation mode is known and transducers configuration can be selected to enhance transduction efficiency of this mode compared to others. The second advantage of an active system is the repeatability of the measurements. Guided waves, however, have the property to be dispersive (Cheeke (2012)), which means their properties depend on the frequency-thickness product. The variations of the parameters as a function of this product are called dispersion curves and can be calculated analytically or semi-analytically (Pavlakovic *et al.* (1997)). This allows to determine the properties of a given mode by the interpretation of dispersion curves; for example, the velocity can be known and the time of flight can be converted in distance, or the dispersion

effect can be removed (Wilcox *et al.* (2001)). Another advantage is the accuracy of the measurements. By becoming active, measurements are repeatable and the detection of a defect is more accurate.

The generation of Lamb waves is an important point of SHM because it will define the sensitivity of the system. The direction of excitation is also important: at low frequency, out-of-plane force is more effective to create antisymmetric modes, whereas in-plane force is more effective in the generation of symmetric modes. Different types of transducers are reviewed by Raghavan and Cesnik (2007). There are commonly two configurations for transducers in guided wave SHM; the pitch-catch and the pulse-echo configuration. The pitch-catch method uses two transducers, one for excitation and one for reception of the signals, whereas the pulse-echo technique uses only one transducer to excite and receive the signals. These guided wave transducers configurations are described and compared by Croxford *et al.* (2007).

A ring of transducers bonded to the plate presented by Cawley *et al.* (2012) for the health monitoring of pipes is commercially available. This article studied a ring of transducers produced as a low profile flexible array that was bonded and clamped in place on the pipe surface, to act as sources and receivers. The entire ring was then sealed in a polyurethane jacket to provide complete protection from the environment. This system is called G-PIMS and is developed and commercialized by Guided Ultrasonics Ltd. It detects changes in the cross section area in the order of 0.25 % in regions distant from features and 0.5 - 0.75 % at others locations (Galvagni and Cawley (2014)).

Fromme *et al.* (2006) used another type of array to generate guided waves: a circular array of 32 transducers for plate monitoring. Here, they are piezoelectric transducers polarized in the thickness direction in order to excite A_0 at a frequency below the cut-off frequency of A_1. A_0 has a much shorter wavelength than S_0 below the A_1 cut-off frequency, so by choosing A_0, the sensitivity and resolution of the detection is

increased. The distance between each transducer should not exceed about a third to half of the wavelength of the desired Lamb wave mode to avoid grating lobes. This condition on space between transducers limits their diameter to a third of the wavelength. Simulated corrosion defects are detected with these permanent systems. In addition an approximate indication on the defect severity is provided by the reflection amplitude.

Clarke *et al.* (2009) achieved a study on a container panel with defects in the form of holes. The detection is done by the A_0 mode at 35 kHz and by the S_0 mode at 100 kHz with a temperature compensation method. An array of nine transducers for both modes is used. In this work, it is shown that the S_0 mode propagated better through corrugations in the structure than the A_0. Thus, S_0 is more suitable for sparse-array guided wave SHM in this type of structure. 5 mm and 10 mm diameter holes were successfully detected in this configuration.

1.1.2 High frequency ultrasonic waves

There is much less literature on high frequency systems for SHM than there is on low frequency systems (using frequencies where only fundamental Lamb modes exist). Working with high frequency signals should enable the detection of smaller defects in the structure as demonstrated by Raghavan and Cesnik (2007).

Masserey and Fromme (2013) studied the fundamental Lamb modes A_0 and S_0 at high frequencies. The growth of a fatigue crack was monitored on the circumference of a 6.35 mm diameter hole in an aluminum plate of 3 mm in thickness. The crack investigated remained smaller than the plate thickness and was positioned at 90° relative to the propagation axis. A_0 and S_0 Lamb modes were generated with a 2.25 MHz sinusoid windowed by a 5 cycles Hann window. A significant drop of approximately 30% in energy was observed before the crack could be optically detected with a microscope; the crack length was estimated to be 0.38 mm (fatigue crack area of less than 0.05

mm²). For a larger crack, a good correlation between the crack length deducted from the energy ratio behind the fatigue crack and from the length provided by fatigue theory prediction was found showing the promising potential of high frequency guided waves for crack sizing.

Chan *et al.* (2015) further developed the study above with the addition of a second layer of aluminum bonded above the first one for the detection of hidden cracks (cracks under a plate). In this study, the excitation was a sinusoid at 1 MHz windowed by a 10 cycles Hann window. There was no significant effect on the signal until the crack grew through the layer. A through layer crack on the second aluminum plate produced a back scattered wave and a reduced-amplitude zone behind the crack.

1.2 Generalities on Ultrasonic guided waves

For a good understanding of guided wave SHM, a grasp of the background theories on ultrasonic waves is necessary.

Shull (2002) defined ultrasonic waves as high frequency sound waves. These waves vibrate at a frequency above 20 kHz (inaudible by humans) and can propagate in fluids and solids. Shull (2002) provides a history of ultrasonic waves. The first mathematical modeling laws governing sound appeared in the late 16th and early 17th centuries in the work of Galileo Galilei and Marin Mersenne. In 1686, Sir Isaac Newton developed the first mathematical theory of sound, interpreting it as a series of pressure pulses transmitted between particles. Later progress of Newton's theory by Euler, Lagrange, and d'Alembert led to the development of the wave equation.

In solids, bulk waves can only propagate far from boundaries where longitudinal and shear waves are uncoupled. When they are near an interface or a boundary with which they can interact, ultrasonic guided waves are generated. The interactions are

reflections, refractions and mode conversions between longitudinal and shear waves. When the longitudinal and the shear waves are coupled, they are called guided waves. Guided waves need interfaces between two materials to travel. They are guided by the boundaries of the structure into which they propagate. There are several types of guided waves. Rayleigh waves travels on the surface of a semi-infinite solid, and were detailed for the first time by Rayleigh (1888). Lamb waves in solids with a thickness of the order of the excitation wavelength were defined by Lamb (1917).

1.2.1 Definitions of signal propagation velocities

Considering the modulation of a sinusoidal wave by a Hann window, the resultant signal is shown in Figure 1.1. The Hann window is the envelope and the resultant signal is the solid line. The signal propagates along the x direction; At a fixed point $x = d$, the amplitude changes over time and at a fixed time t, the amplitude changes over the propagation distance x.

The phase velocity is the propagation speed of a given phase, meaning the propagation of a single frequency component of a harmonic wave. For example, for the wave defined above, the phase velocity corresponds to the propagation velocity of a fixed point on the signal curve as represented in Figure 1.2 by the blue point chosen here as a crossing-zero point. The wave travels the distance d in a time Δt_{ph} as shown in Figure 1.2, hence the propagation speed this is $c_{ph} = \frac{d}{\Delta t_{ph}}$. This velocity is called phase velocity phase velocity.

The group velocity corresponds to the propagation speed of the energy or information contained in the wave. This means that the group velocity is the velocity with which the overall wave amplitude travels, or the velocity of a fixed point on the envelope as represented in Figure 1.2 by the black point arbitrarily determined for this example.

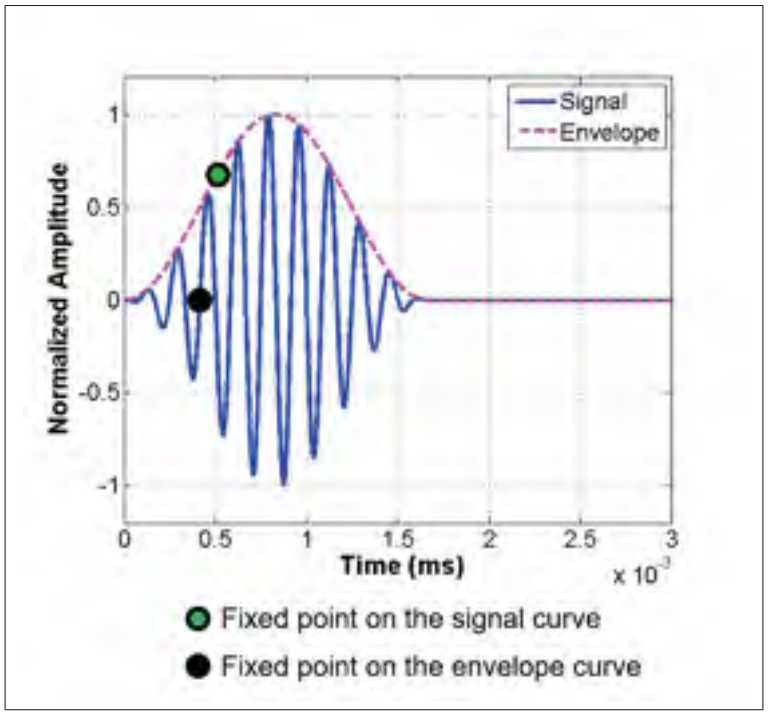

Figure 1.1 Time representation of the signal modulation; the dashed line is the envelop and the solid line is the signal

The envelope travels the distance d in a time Δt_g, hence the envelope speed is $c_g = \frac{\Delta t_{ph}}{T}$. This speed is called the group velocity.

1.2.2 Propagation of guided waves in solids

The propagation of elastic waves is well documented, and the development to obtain the wave equation is detailed by Rose (1999), Cheeke (2012) and Graff (1991). A general view is provided here with the principal governing equations and essential characteristics.

Guided waves are an important class of waves that have widespread applications in SHM. These waves can travel long distances with low attenuation. Therefore, they are highly appropriate for plate inspection.

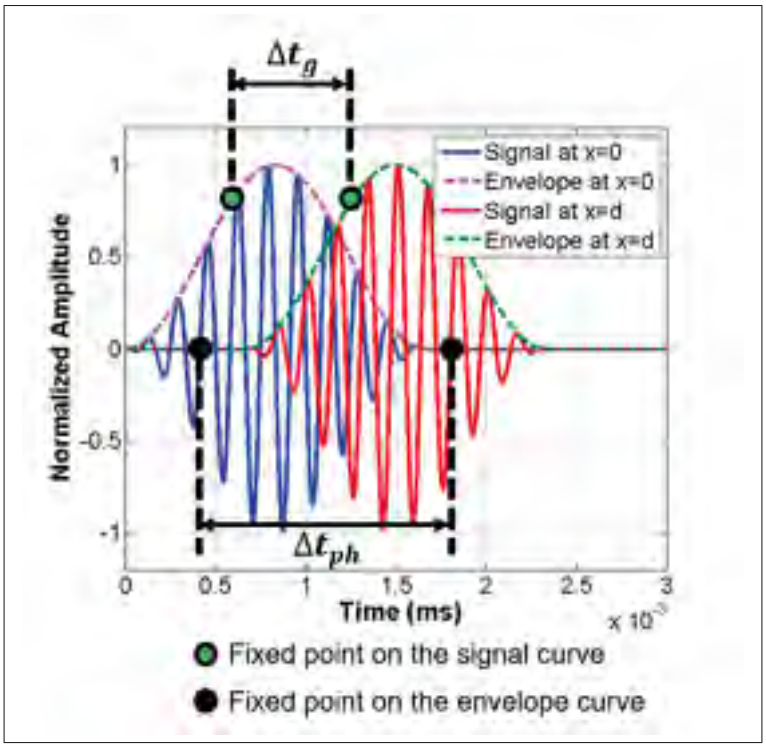

Figure 1.2 Signal before propagation (x=0) and after a propagation distance d (x=d) for phase and group velocity definition

The 3D elastic theory governs wave propagation in solids. In an unbound elastic body, waves propagate freely in all directions. There are, however, two modes of propagation: the Longitudinal-wave (L-wave) mode and the Shear-wave (S-wave) mode. When the wave propagates in the L-wave mode, compressional stresses are generated in the solid and the wave propagation speed is:

$$c_L = \sqrt{\frac{\lambda + 2\mu}{\rho}} \qquad (Longitudinal\ wave\ speed) \tag{1.1}$$

Where λ and μ are the Lamé coefficients and ρ the material density. When the wave propagates in the S-wave mode, shear stresses are generated and the propagation speed is:

$$c_S = \sqrt{\frac{\mu}{\rho}} \qquad (Shear\ wave\ speed) \tag{1.2}$$

In a bounded structure the S-waves are separated into two categories of waves: the Shear-Vertical (SV) and the Shear-Horizontal (SH) waves. Shear-Horizontal waves have a particle motion contained in the horizontal plane xOz, as defined in Figure 1.3. Lamb waves are coming from the interactions between SV-waves, which are S-wave polarized in the plane yOz as defined in Figure 1.3, L-waves and boundaries in a plate.

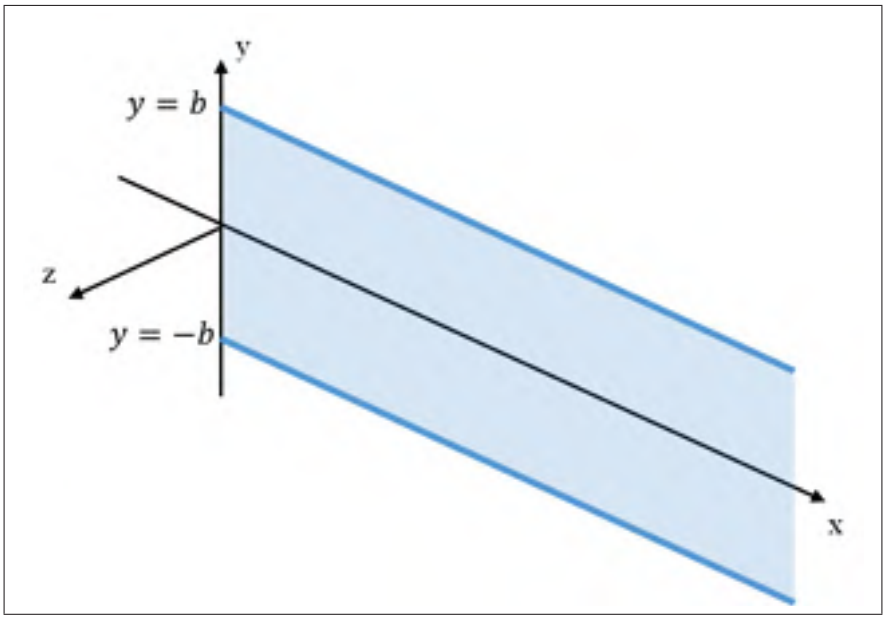

Figure 1.3 Schematic representation of an infinite plate according to x and z of thickness $2b$ with surface at $y = b$ and $y = -b$

There are two techniques to determine guided wave equations; the partial wave technique developed by Solie and Auld (1973) and the potential technique by Lamb (1917). Lamb waves and SH waves are presented below.

1.2.2.1 Governing equations of SH waves in plates

SH modes are the simplest case because there is only one direction of polarization and because they are decoupled from the sagittal modes which are the modes polarized in the xOy plane defined in Figure 1.3; therefore there is no mode conversion or reflection.

The mathematical definition of SH waves in plates presented here is summarized from Cheeke (2012).

citedavid2002fundamentals and Giurgiutiu (2014) use the partial wave technique to establish SH wave equation. SH waves have particle motion along the z-axis and wave propagation along the x-axis, as represented in Figure 1.4.

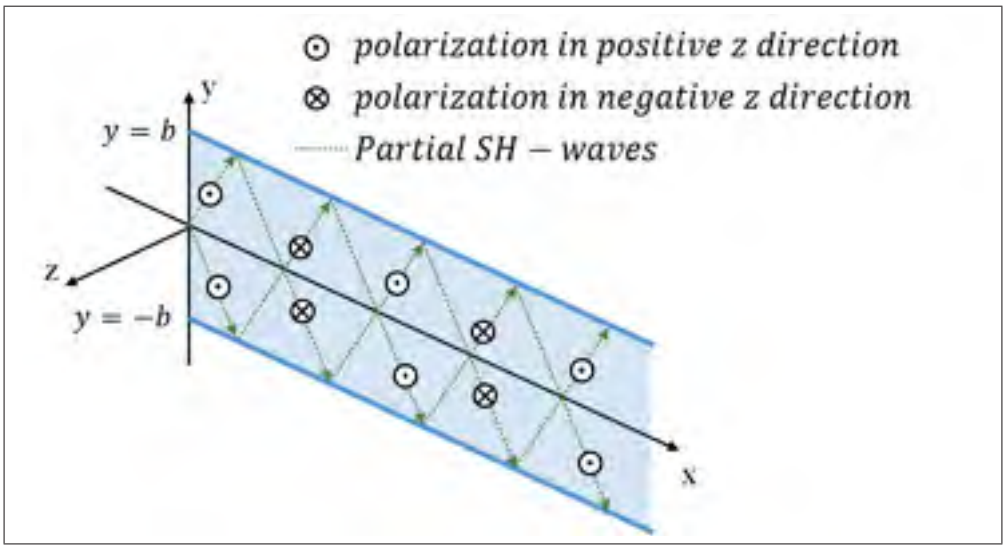

Figure 1.4 Representation of partial waves for the SH wave equation

The propagation of these waves is governed by the following equation:

$$c_{ph_{SHm}} = \frac{c_S}{\sqrt{1-(\frac{m\pi}{2b})^2(\frac{c_S}{\omega})^2}}, \qquad m = 0, 1, 2, ... \tag{1.3}$$

Where $c_{ph_{SHm}}$ is the phase velocity of the mode of order m, c_S the shear wave speed and ω the angular frequency. $c_{ph_{SHm}}$ is a function of ω, which means that SH waves are dispersive except for the 0-th order as $c_{ph_{SH_0}} = c_S$ is constant over the frequency.

The curves of phase velocity as a function of frequency are determined by Equation 1.3. These curves are computed analytically with the software Disperse, developed by Pavlakovic *et al.* (1997); and are represented in Figure 1.5.

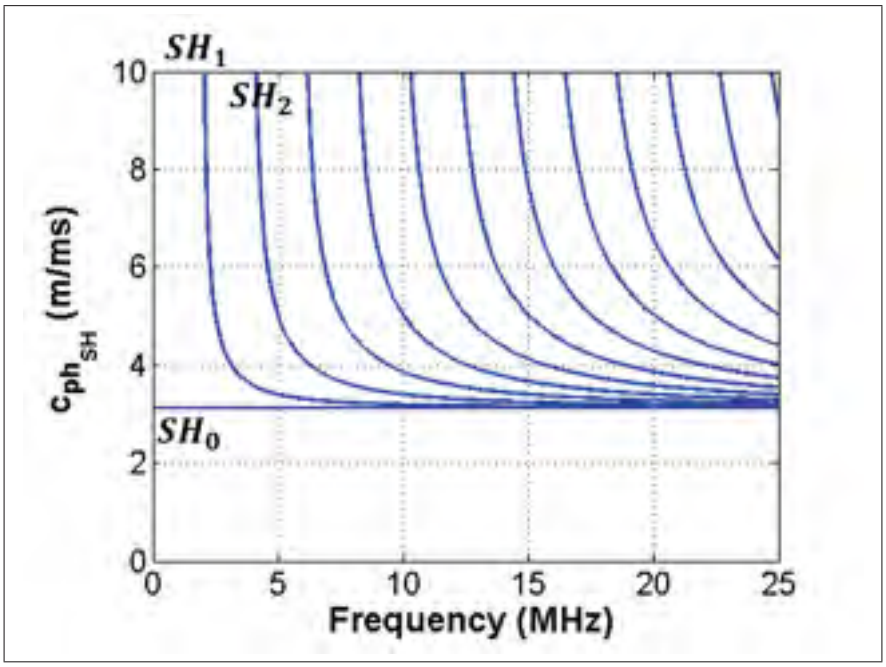

Figure 1.5 Dispersion curves of phase velocity for symmetric SH waves in a 1.6 mm thick aluminum plate extracted from Disperse

The group velocity is the derivative of frequency with respect to wavenumber k,

$$c_{g_{SH_m}} = \frac{d\omega}{dk} = \frac{c_S^2 k}{\omega} = \frac{c_S^2}{c_{ph_{SH_m}}} \tag{1.4}$$

As seen with the phase velocity, the SH waves are dispersive except the SH_0 mode, and thus the group velocity varies with the frequency. The curves of group velocity are represented in Figure 1.6.

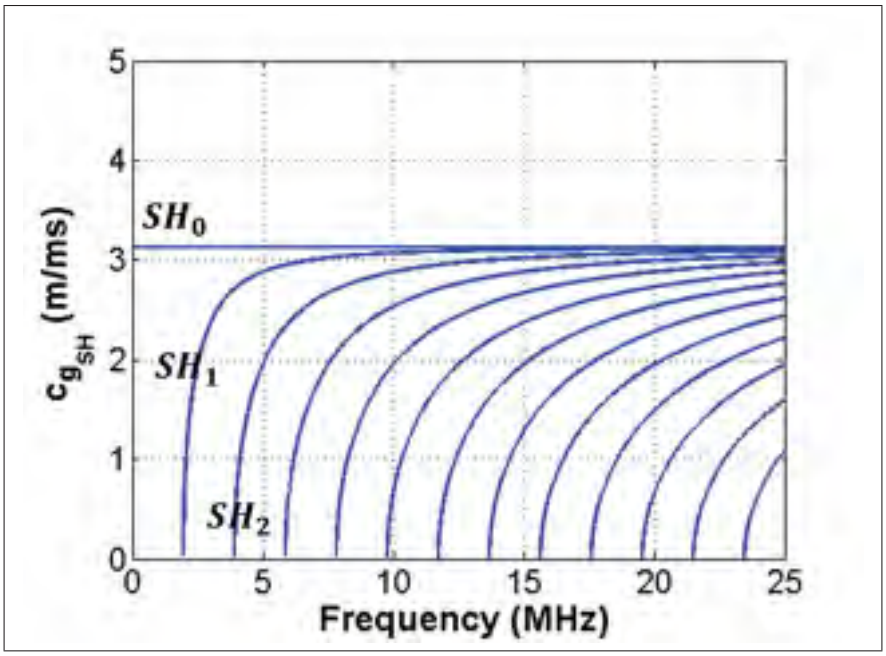

Figure 1.6 Dispersion curves of group velocity for symmetric SH waves in a 1.6 mm thick aluminum plate extracted from Disperse

1.2.2.2 Governing equations of Lamb waves in plates

Vertically polarized shear waves (SV-waves) and longitudinal waves (L-waves) simultaneously exist in a plate, as is represented in Figure 1.7. Lamb waves are the result of multiple reflections as well as constructive and destructive interferences between the L-waves and SV-waves. The partial wave technique is used here to determine the Lamb wave equations. The partial waves are composed of pressure (longitudinal) and shear vertical waves. In plates, L-waves and SV-waves are coupled and inseparable.

The symmetric modes of Lamb waves are designated S_0, S_1, S_2,... and the antisymmetric modes are designated A_0, A_1, A_2,.... The movement of particles in symmetric and antisymmetric modes are illustrated in Figure 1.8.

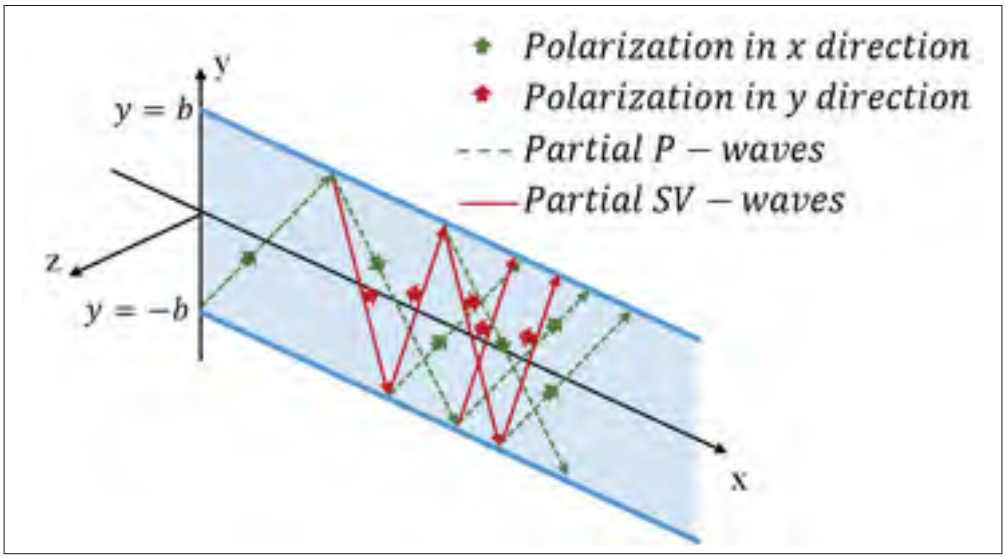

Figure 1.7 Representation of partial waves used in the isotropic problem

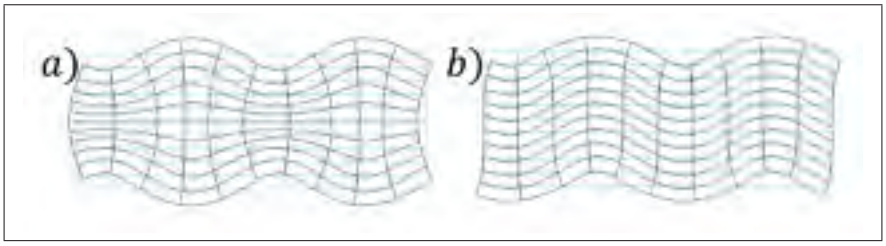

Figure 1.8 Displacement of particles for a) symmetric modes and b) antisymmetric modes (source: Disperse)

The Lamb waves are governed by the Rayleigh-Lamb equation, which is detailed by Cheeke (2012). For symmetric modes:

$$\frac{\tan(pb)}{\tan(qb)} = -\frac{(k^2-q^2)^2}{4k^2pq} \tag{1.5}$$

And for antisymmetric modes:

$$\frac{\tan(pb)}{\tan(qb)} = -\frac{4k^2pq}{(k^2-q^2)^2} \tag{1.6}$$

Where k is the wavenumber and can be expressed as $k = \frac{\omega}{c_{ph}}$. The transverse wave vector components are linked to ω and the wave vector k by:

$$p^2 = \left(\frac{\omega}{c_L}\right)^2 - k^2 \tag{1.7}$$

and

$$q^2 = \left(\frac{\omega}{c_S}\right)^2 - k^2 \tag{1.8}$$

These equations are solved semi-analytically by Disperse (Pavlakovic *et al.* (1997)). The solutions are functions of ω; thus, Lamb waves are also dispersive. The dispersion curves for the phase velocity obtained with Disperse are shown in Figure 1.9

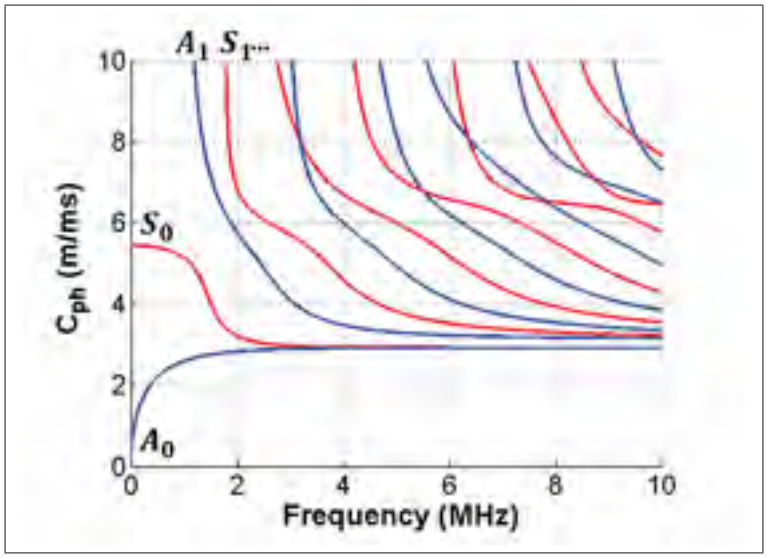

Figure 1.9 Dispersion curves of Lamb waves phase velocity for a 1.6 mm thick aluminum plate extracted from Disperse

The group velocity shown in Figure 1.10, can be derived from phase velocity, through the relation:

$$c_g = c_{ph}^2 \left(c_p ph - fb \frac{\partial c_{ph}}{\partial fb} \right)^{-1} \tag{1.9}$$

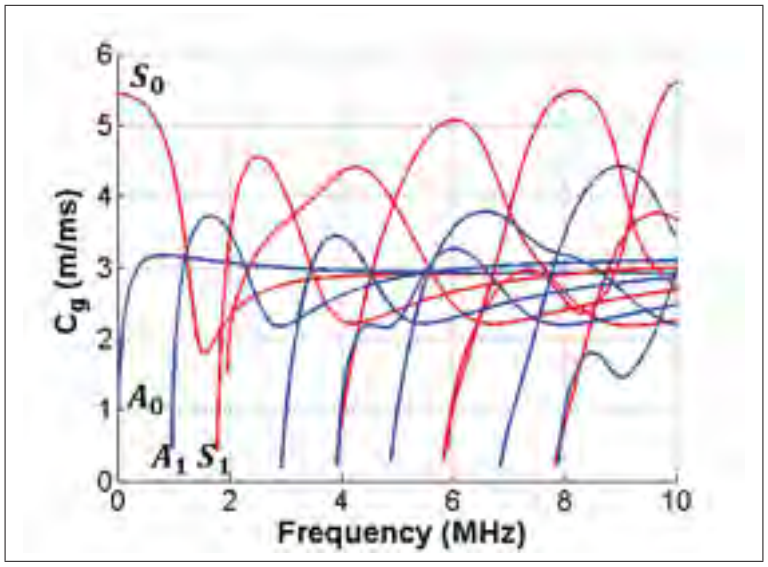

Figure 1.10 Dispersion curves of Lamb waves group velocity for a 1.6 mm thick aluminum plate extracted from Disperse

1.2.3 Effects of the dispersion on Lamb waves

Due to their dispersive nature, Lamb wave signals are deformed through propagation. Each frequency component in the wave travels at its own velocity. The velocities of every mode at every frequency can be determined on the dispersion curves, presented in Figures 1.9 and 1.10. For example, a 10-cycle Hann-windowed toneburst centered at 4 MHz, shown in Figure 1.11, generated in a 1.6 mm thick aluminum plate is deformed during its propagation. The deformation is due to the propagation of multiple modes which travel at different velocities and the different velocities of each frequency component of each mode.

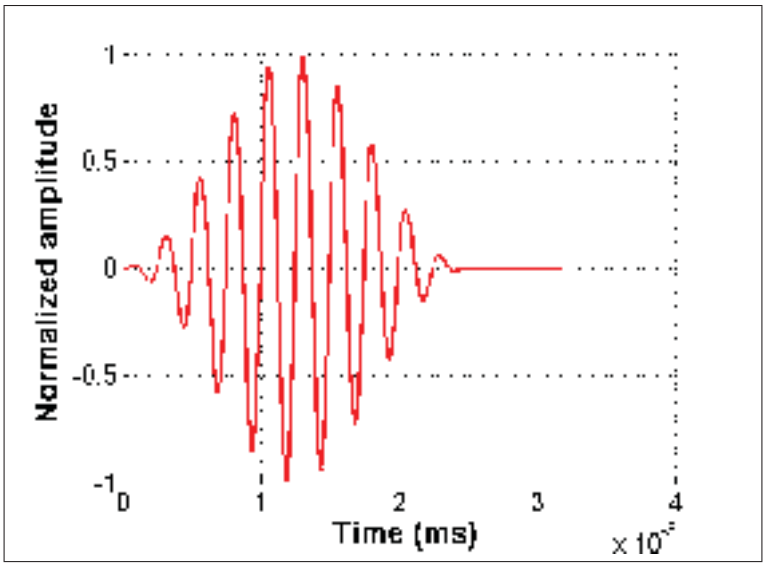

Figure 1.11 Out-of-plane displacement 10-cycle Hann-windowed toneburst at 4 MHz

As determined on the dispersion curves, there are approximately eight modes able to propagate in this structure at this central frequency. The wave deformation is shown in Figure 1.12 after five propagation distances: 50 mm, 100 mm, 200 mm, 500 mm and 1000 mm. The frequency components are also shown on this figure.

The dispersion and the superposition of multiple modes are visible in the time representation of the signal after 500 mm of propagation shown in Figure 1.13. The temporal spreading illustrates the propagation of different modal components, and in each modal component the frequency components travel at different velocities and each mode is deformed separately. The frequency composition of a mode does not vary over the propagation distance, as shown in Figure 1.12.

In addition, the superposition of all the modes prevents one from differentiating the modes. As illustrated in Figure 1.13, the modes are superposed. The ratios between mode amplitudes and the excitation amplitude are presented in Figure 1.14

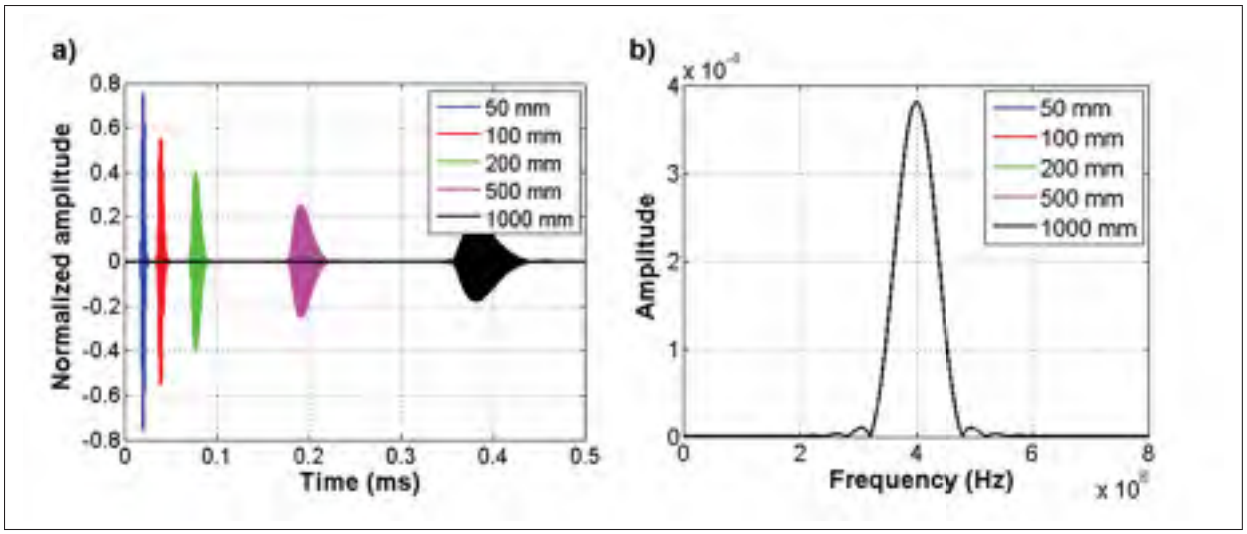

Figure 1.12 Propagated forms of A_1 generated by a 10-cycle Hann-windowed toneburst at 4 MHz; a) Time representations and b) the frequency componenent for different propagation distances

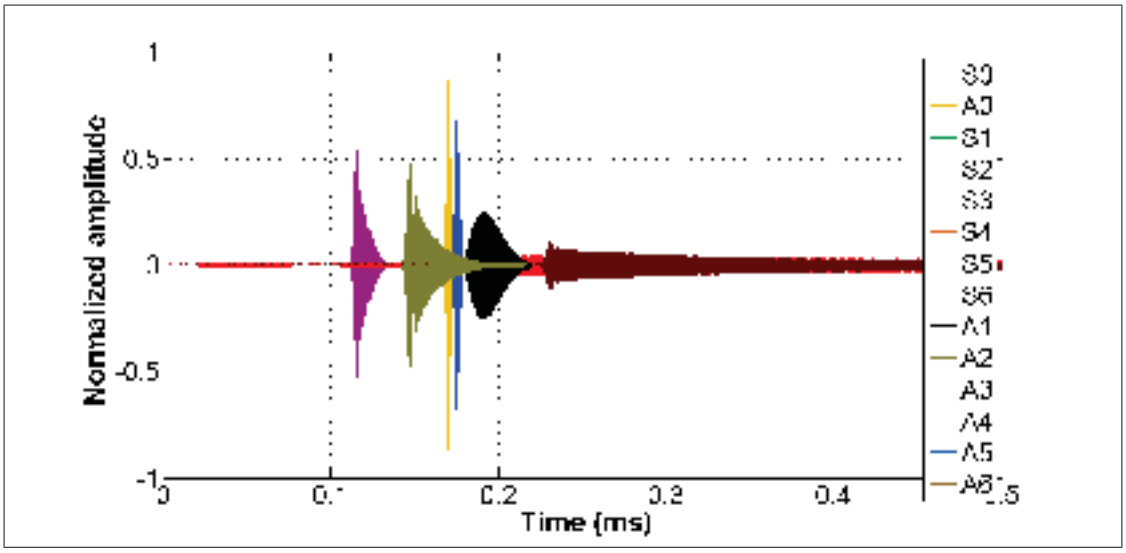

Figure 1.13 Propagated form of a 10-cycle Hann-windowed toneburst at 4 MHz after 500 mm with differentiation of each mode

Working with high order Lamb wave modes implies complex signals, and requires signal processing techniques that enable the comparison of signals and the separation of the modes propagating within the structure under study.

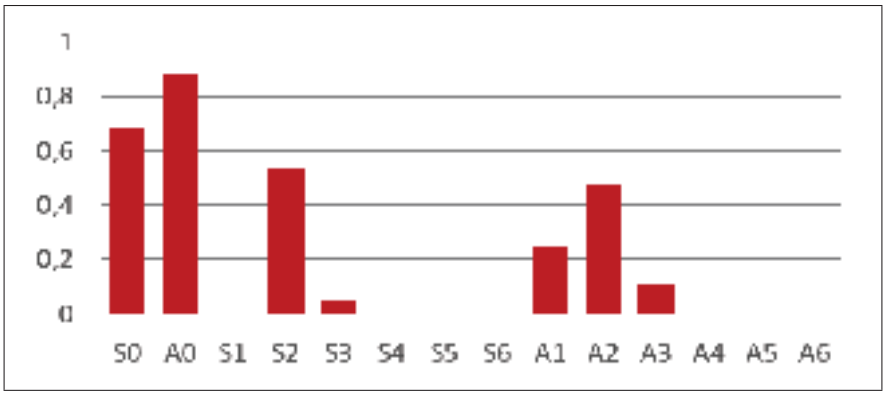

Figure 1.14 Ratios between mode amplitudes and excitation amplitude for modes propagating from a 10 cycle toneburst at 4 MHz after 500 mm of propagation in a 1.6 mm thick aluminum plate

1.3 Signal processing

1.3.1 Correlation function

The correlation function provides a level of similarity between a signal and a different signal delayed in time. This means that for each time delay applied to the second signal, the correlation function provides a value that represents the level of resemblance. This function is used to achieve signal subtractions with deleting any undesired time delay. If this function is applied on a propagating signal A at $t = 0$ and the same signal after propagation, the traveling time would correspond to the highest value of the correlation function.

For example, a signal and its propagated version are represented in Figure 1.15 and are compared with the correlation function. The result of this function is the last graphic in Figure 1.15, which shows two maximums at different symmetric delay values with respect to zero. This means that the second signal is delayed by $500 samples$ from the first one. The function enables to determine the level of similarity between two signals, or the period of a signal. When dealing with a high level of noise like in the example, the delay or the period can be precisely determined with this technique.

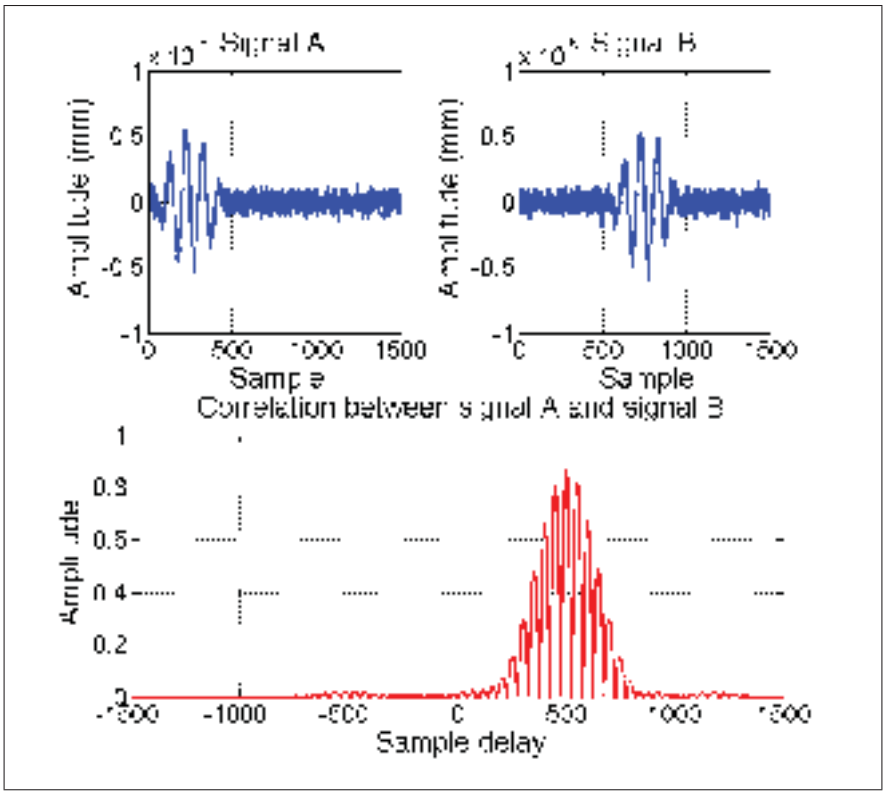

Figure 1.15 Correlation between a) a signal A and b) a delayed version of signal A (Signal B) and c) the results of the correlation between signal A and B

1.3.2 Frequency-wavenumber representation

The propagating modes must be identified and separated in order to analyze them independently. The frequency-wavenumber representation is obtained from a 2D Fourier transform–a technique developed by Alleyne and Cawley (1991). This method consists of applying a Fourier transform of the time history of the response at each monitored spatial point; which results in the spectral information for each output. Then a spatial Fourier transform is applied on the components at a given frequency. Finally, the result is a 2D array of amplitudes at discrete frequency and wavenumbers. This method enables the amplitudes and velocity of different modes propagating at the same frequency to be determined. The 2D Fourier transform is used to identify the multiple Lamb wave modes that propagate within a structure.

This representation allows to analyze a signal during its spatial propagation, and also during its time propagation - therefore enabling the processing of mode superposition due to the dispersion of Lamb waves and reflections. Multiple points of measurement are however required to obtain the signal evolution in space and time.

For example, the representation of this signal in the frequency-wavenumber plane for a 10-cycle Hann-windowed signal at 4MHz during its propagation is shown in Figure 1.16. Each line with a significant amplitude represents a propagating mode. This representation takes positive and negative wavenumbers into account, enabling to differentiate modes propagating in the positive direction of the propagation axis ($wavenumbers < 0$) from modes propagating in the negative direction ($wavenumbers > 0$).

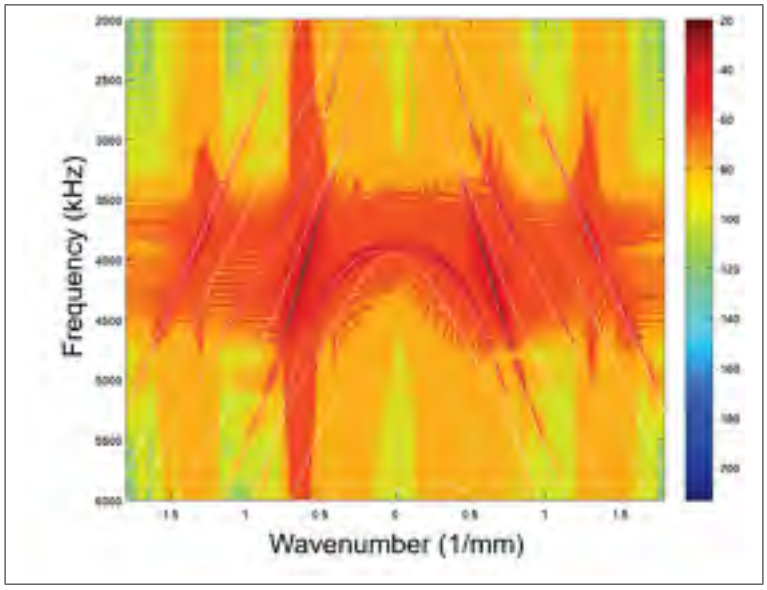

Figure 1.16 2D Fourier transform of a 10-cycle Hann-windowed in-plane signal at 4MHz in a 1.6 mm thick aluminum plate

The frequency-wavenumber representation is used in this thesis to identify the multiple modes propagating and to analyze them independently. However, the quality of

this representation depends upon several parameters such as the space step between the monitored positions, the total length of monitored points, the time step in measurements and the total time of measurement. The space step governs the maximum wavenumber on the plane, and the total length controls the wavenumber resolution. The same rules applies on the frequency axis with time variables. If the maximum wavenumber value is not high enough, the lines representing the modes are overlaid, and a low resolution affects the power of separation for two close modes.

In addition, working at a high frequency with guided waves increases the wavenumbers. Finite element simulations do not meet problems with applying small space steps, but experimentally it could be too complex or even impracticable to reach certain space step values.

CHAPTER 2

FINITE ELEMENT MODELING

In this chapter, ultrasonic guided waves were simulated with the commercial finite element software Abaqus and a non-commercial software Pogo developed by Huthwaite (2014). Pogo uses the same finite element equations as Abaqus in the problem resolution. Pogo runs its calculations on the Graphical Processor Units (GPU's) instead of the computer Central Processor Units (CPU's). This allowed to parallelize the simulation on multiple cores at a lower price than it would with the same amount of CPU's.

The explicit scheme was used to solve the elasto dynamic equations governing the propagation of elastic waves. Pogo and Abaqus gave the same final results as demonstrated by Huthwaite (2014).

In order to be as close as possible to reality and to keep an acceptable computation time, the following parameters were carefully selected: the type of elements, the maximal element size admitted, the time increment, and the time period of the simulation. These parameters must respect certain properties and follow certain rules to obtain accurate simulation results in a reasonable time.

2.1 FE modeling for guided waves

The finite element simulations are based on an assumption of linear elasticity. The general equation of motion in a matrix form is:

$$\boldsymbol{M}\ddot{\boldsymbol{u}} + \boldsymbol{C}\dot{\boldsymbol{u}} + \boldsymbol{K}\boldsymbol{u} = \boldsymbol{F}_a \tag{2.1}$$

Where $\boldsymbol{M}$ is the structural mass matrix, $\boldsymbol{C}$ is the structural damping matrix, $\boldsymbol{K}$ is the structural stiffness matrix, $\boldsymbol{F}_a$ is the vector of external loads and $\boldsymbol{u}$, $\dot{\boldsymbol{u}}$ and $\ddot{\boldsymbol{u}}$ are the displacement vector and its time derivatives.

The attenuation was not considered in this thesis since it is low in metallic material and the studied structure is in aluminum. Equation 2.1 is solved by Abaqus and Pogo using the dynamic explicit integration scheme also called the forward Euler scheme.

The 2D and 3D finite element models were built with two-dimensional or three-dimensional quadrilateral elements with linear reduced integration. They are the basic elements for regular geometry and excitation and by assuming that the problem is linear these elements give the best compromise between accuracy and rapidity as demonstrated by Drozdz (2008). In addition, these elements provide good results for crack modeling, according to the study by Drozdz (2008).

The computation was performed in the time domain in order to represent the experimental setup.

The material used was aluminum with mechanical properties extracted from the software Disperse and presented in Table 2.1.

Table 2.1 Recap of Aluminium properties used

Modulus of elasticity	**Poisson coefficient (ν)**	**Density**
70.8 GPa	0.34	2700 kg/m^{-3}

2.1.1 Element size

The maximal element size in a model defines the maximal error made in the simulation as studied by Drozdz (2008). Modeling with smaller elements improves the discretization

of the structure by reducing the space step between each node. The higher the number of elements, the longer the computation time; hence a compromise must be found between accuracy and computation time by acting on the element size.

The size of a square element is defined as the length of one side as represented in Figure 2.1. In order to reduce the time of calculation, an optimal element size has to be determined.

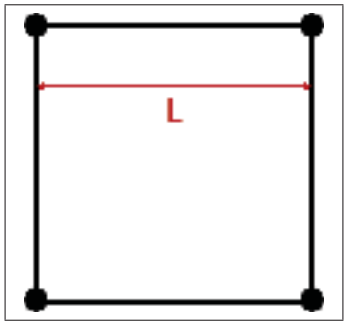

Figure 2.1 Definition of mesh size for a square element

Simulations with different mesh sizes were run on Pogo to determine the error made as a function of the ratio of elements per wavelength.

The structure under study was a 1.6 mm thick and 150 mm long two-dimension plate. Examples of the mesh in the thickness are shown in Figure 2.3. The material is an aluminum with the properties previously defined in 2.1. In addition, the reflexions were removed by windowing the signal.

The values of the number of elements per wavelength varied from 5 to 50, and the excitation was a 10-cycle Hann windowed sinusoid centered at 4 MHz, as shown in Figure 2.2.

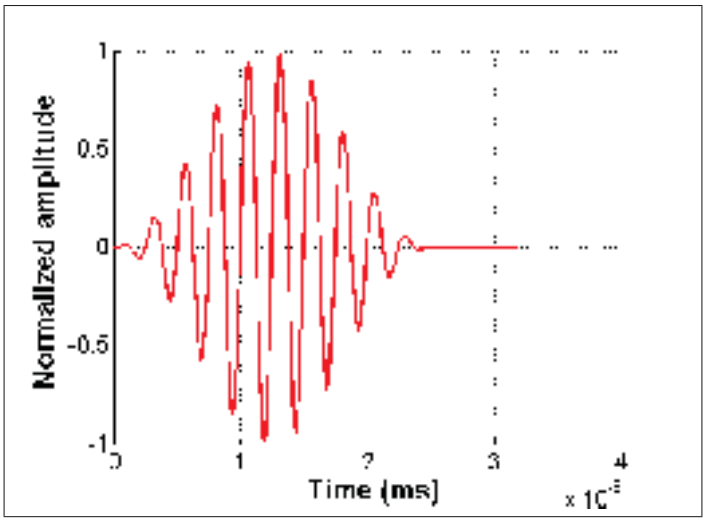

Figure 2.2 Time representation of a 10-cycle Hann-windowed sinusoid centered at 4 MHz

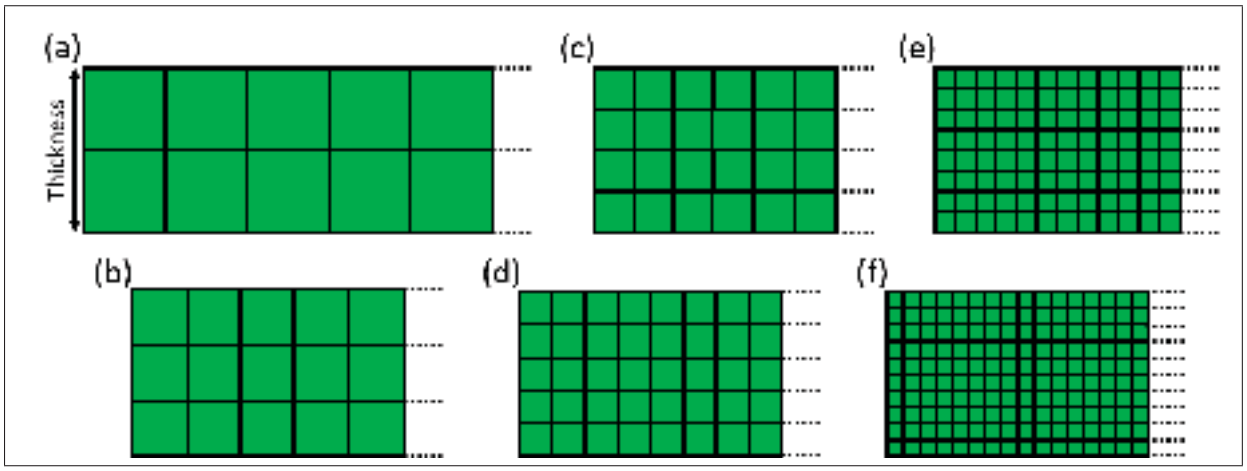

Figure 2.3 Examples of 1.6 mm thick plate models used for the element size study (a) 0.8 mm (b) 0.53 (c) 0.4 mm (d) 0.32 mm (e) 0.2 mm (f) 0.16 mm

To determine the error made in the simulations, the wavenumber components at 4 MHz for the incident S_0 mode extracted from simulations were compared with the values provided by Disperse, which compute semi-analytically the dispersion curves. More specifically, the post-processing consists of the study of the two-dimensional Fast Fourier Transforms (2D FFT) developed by Alleyne and Cawley (1991). These

representations were compared to the theoretical dispersion curves from Disperse. Examples of comparisons are shown in Figure 2.4. The S_0 and S_1 modes did not exist in Figure 2.4 a) whereas they begin to appear in the Figure 2.4 b). Although the S_2 and S_3 modes appeared in Figures 2.4 a) and b), they were closer to the theory in Figure 2.4 b). However, the definitions of S_0 and S_1 were not accurate enough considering the maximal acceptable error fixed at 2%.

The error was obtained by subtracting the wavenumber value provided by Disperse for the incident S_0 mode at 4 MHz from the wavenumber coordinate of the maximum value in the 2D FFT at 4 MHz for the same mode.

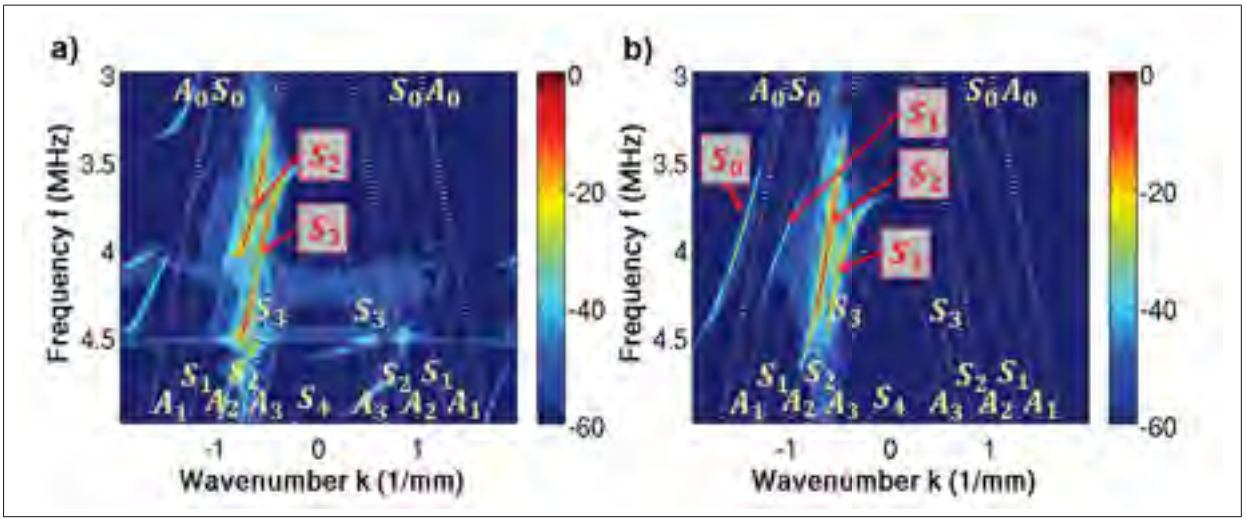

Figure 2.4 Comparison between the 2-dimensions Fast Fourier Transform for (a) element size of 0.2 mm (3.5 elements/wavelength) and (b) 0.145 mm (5 elements/wavelength); dispersion curves from Disperse in gray

The analysis of the error enabled the determination of a minimal ratio of element per wavelength in order to be obtain accurate simulation results. The ratio has to be superior to 10 to obtain a maximal error of 2% for S_0, as shown by the curve of error as a function of the number of element per wavelength in Figure 2.5. The maximum ratio

must be selected to provide a reasonable computation time, the value chosen for this thesis was 20. In addition, considering that S_0 has the highest wavelength amongst the symmetric modes propagating at 4 MHz, the errors made on the high order modes were inferior to 2% with the range of ratio previously defined.

A ratio of number of elements per wavelength within the range previously defined enabled to compute simulation, making an acceptable error on the mode propagation. The range for the acceptable number of elements per wavelength ratio determined corresponds to the results presented by Drozdz (2008).

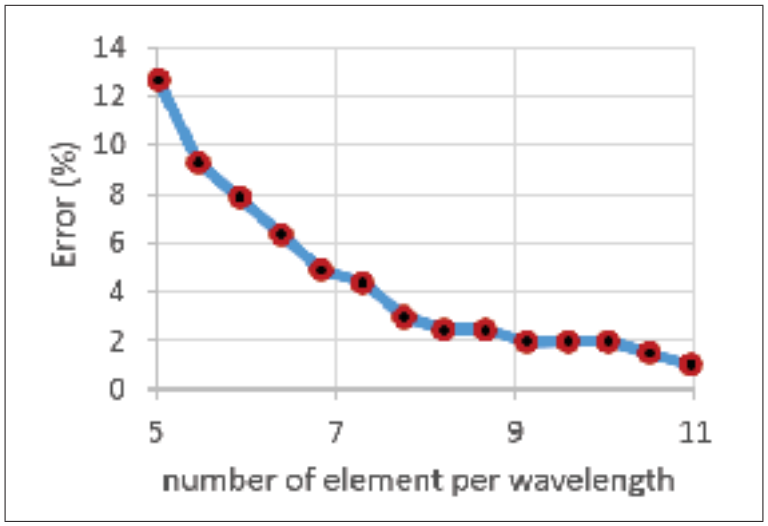

Figure 2.5 Curves of error in % between theory and simulation as a function of the ratio number of elements per wavelength at 4 MHz for the S_0 mode

2.1.2 Time increment and Time period

In addition to an adequate element size, the time increment has to be selected wisely to ensure the stability of the simulations. The time increment must satisfy the Courant-Friedrichs-Lewy (CFL) condition defined in Cook *et al.* (2007). The CFL condition prevents the wave from traveling completely through one element during a single time

increment. The time increment, Δt, must be smaller than the critical time step, Δt_{cr}. The critical value depends on the maximal phase velocity propagating in the smallest element, as defined in Equation 2.2.

$$\Delta t \leqslant \Delta t_{cr} = 0.8 \frac{\Delta L}{c_{ph_{max}}} \tag{2.2}$$

Where $c_{ph_{max}}$ is the maximal phase velocity and ΔL is the size of the smallest element and 0.8 a security factor.

In addition, the condition on the number of elements per wavelength ratio implies a condition on the time increment. The minimal ratio of 10, provides:

$$\frac{\Delta x}{\lambda_{min}} \leqslant \frac{1}{10} \tag{2.3}$$

Where Δx is the maximal element size and λ_{min} the minimal wavelength in the propagating signal. Considering that $\lambda_{min} = \frac{c_{ph_{min}}}{f_{max}}$, Equation 2.3 leads to:

$$\Delta t \leqslant \frac{1}{10 f_{max}} \tag{2.4}$$

Equations 2.2 and 2.4 are the two conditions to verify to ensure the stability of the simulations.

2.2 Absorbing layers

Absorbing layers are implemented at the structure boundaries in order to avoid reflections from the structural features. Absorbing layers constitute a region added to the extremities of models to simulate an unbounded structure as defined by Rajagopal *et al.* (2012). This is illustrated in Figure 2.6. These additional layers are designed to absorb any wave entering them, thus avoiding the reflection from the structure boundaries.

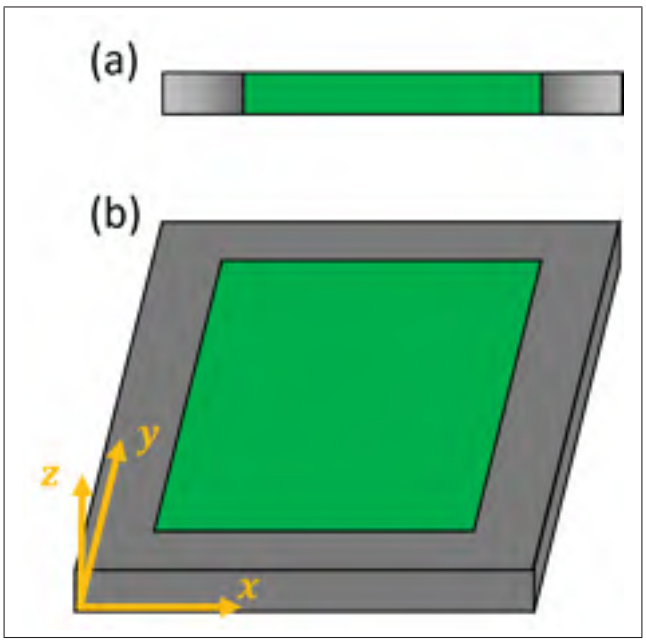

Figure 2.6 Absorbing layer concept representations for (a) 2-D and (b) 3-D plate model

Their objective is to approximate an unbounded medium problem by absorbing waves traveling across them. Small reflections coming back from the absorbing region can exist, but they are made negligible with a correct definition of the layer's parameters.

Two techniques exist to implement absorbing regions. The first one is called the Perfectly Matched Layer (PML) technique, which is mainly used in frequency-domain analyses. This method was not used in this master's thesis since the work was done in

time domain-but it is detailed by Rajagopal *et al.* (2012) and Drozdz *et al.* (2007). The second method is called the Absorbing Layer with Increasing Damping method (ALID), which was used in this thesis and is presented below. This second technique has the advantage of a much easier implementation.

The ALID method consists of adding a region composed of several layers of a material that has the same mechanical properties as the adjoining structure, except for the value of the viscous damping, α. This damping (also called mass damping) is a mass proportional damping as defined below in Equation 2.7. The α damping value is gradually increased in the layers. The minimal value corresponds to the layer in contact with the studied structure and the material of the extremity layer has the maximum damping value.

The difference between the damping values of consecutive layers results in reflections at every interface between absorbing layers. But the reflections can be minimized by decreasing the damping difference between consecutive layers. This enables to have two materials with more similar mechanical properties, which means that the impedance differences are reduced and thus the reflection at each interface is minimized.

In addition, it is recommended to have one-element-thick layers to have a model size as small as possible and to reduce the computation time.

The mathematical definition of the ALID presented by Drozdz (2008) begins with the equilibrium equation in the time domain, assuming time harmonic waves:

$$-[\boldsymbol{M}]\omega^2 u - [\boldsymbol{C}]i\omega u + [\boldsymbol{K}]u = F_a, \tag{2.5}$$

where $[\boldsymbol{M}]$, $[\boldsymbol{C}]$ and $[\boldsymbol{K}]$, are respectively the mass, damping and stiffness matrices and F_a the applied loads. The Rayleigh damping, proportional to stiffness or mass, can be

introduced in most FE packages. If we define $[\boldsymbol{C}] = \alpha[\boldsymbol{M}] + \beta[\boldsymbol{K}]$, where α and β are the mass and stiffness proportionality coefficients, we can rewrite Equation 2.5:

$$-[\boldsymbol{M}]\left(1+i\frac{\alpha}{\omega}\right)\omega^2 u + [\boldsymbol{K}](1-i\omega\beta)u = F_a \tag{2.6}$$

In the case of Absorbing Layers with Increasing Damping with a boundary perpendicular to the x-axis defined in Figure 2.6, the value of α and β are gradually increased in the x-axis direction. We set the following formulation:

$$\alpha(x) = \alpha_{max} \cdot X(x)^p \qquad and \qquad \beta(x) = \beta_{max} \cdot X(x)^p \tag{2.7}$$

α_{max} and β_{max} are positive real numbers and X is a function varying from 0 at the layer in contact with the structure to 1 at the extremity of the absorbing region. X follows a power law whose order is defined by p. In the time domain, α_{max} and β_{max} are constant.

The effect of Rayleigh damping can be better understood by introducing a formulation using complex density and stiffness modulus in the ALID definition:

$$\rho_{ALID} = \rho\left(1+i\frac{\alpha(x)}{\omega}\right) \qquad and \qquad E_{ALID} = E(1-i\omega\beta(x)) \tag{2.8}$$

The use of damping, however requires to have a smaller time increment to achieve a stable simulation with an explicit solving scheme. A high value of α causes a relatively small decreasing of the stable time increment whereas a high value of β strongly affects the stable increment (divided by thousand or more). It is preferable, therefore, to use only α to define ALID with an explicit scheme. The suggested value for p is 3, and a good combination between the total length of absorbing region and α_{max} has to be found case-by-case. In addition, $X(x) = \lfloor \frac{x}{L} \rfloor$ with L the total length of the absorbing region and x the position relative to the beginning of this region (the function $\lfloor \ \rfloor$ is the integer part)

CHAPTER 3

CRACK DETECTION USING LOW FREQUENCY GUIDED WAVES

This section presents a study of the capability of low frequency Lamb waves to detect cracks on the circumference of a through-thickness hole in a 1.6 mm thick plate. The dimensions of the inspected plate were 305 mm x 305 mm x 1.6 mm, as shown in Figure 3.1.

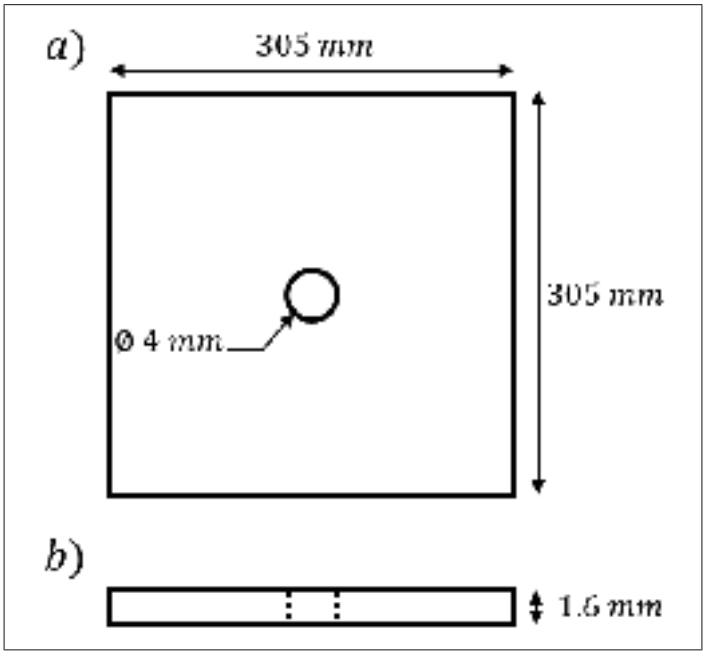

Figure 3.1 Plan of the model under study a) top view and b) front view

Working with low frequencies means that the frequency components of the excitation signal are below the A_1 cut-off frequency. In this region, only the fundamental modes can propagate within the structure, as shown in Figure 3.2 in Zone 1. For a 1.6 mm thick plate made of aluminum, only fundamental modes can propagate at a frequency below approximately 1 MHz. This property of the Lamb waves makes the

excitation generation and the post processing more convenient, as the modes can be mostly generated and identified in the results analysis with ease.

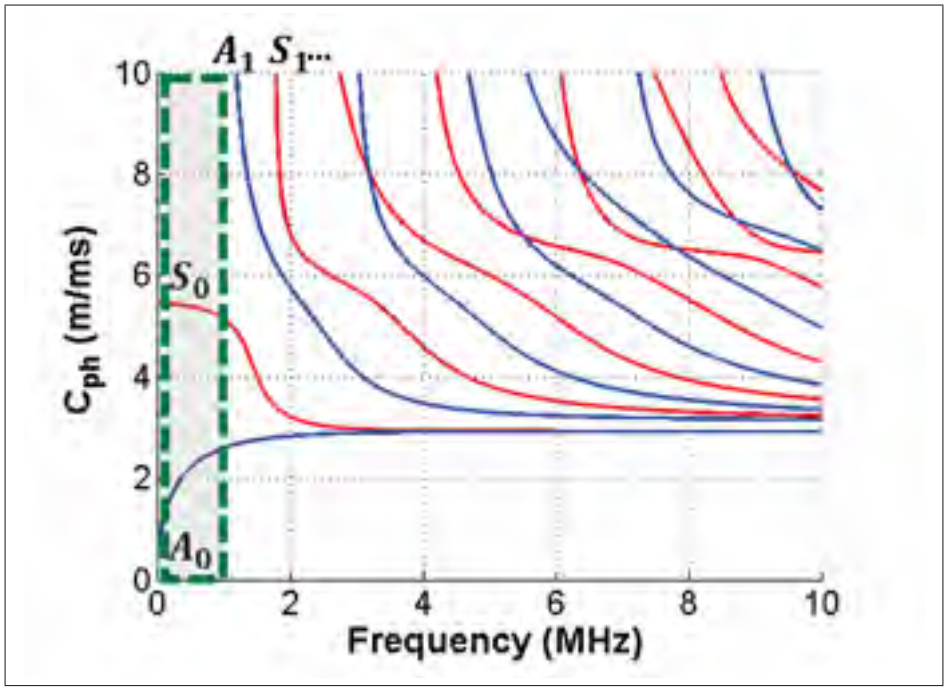

Figure 3.2 Dispersion curves of Lamb waves phase velocity for a 1.6 mm thick plate made of aluminum with low frequency zone in the rectangle

The study investigated the influence of some crack parameters, such as the length and the orientation, on the interactions between crack and fundamental Lamb wave modes. The position of the crack was defined by its orientation relative to the X-axis, and the size was defined by the length. The definition of these parameters is detailed in Figure 3.3.

The objective of this section is to determine a method in order to detect and characterize a crack using fundamental Lamb modes at low frequency, and furthermore to identify the limits of the low frequency detection in this configuration.

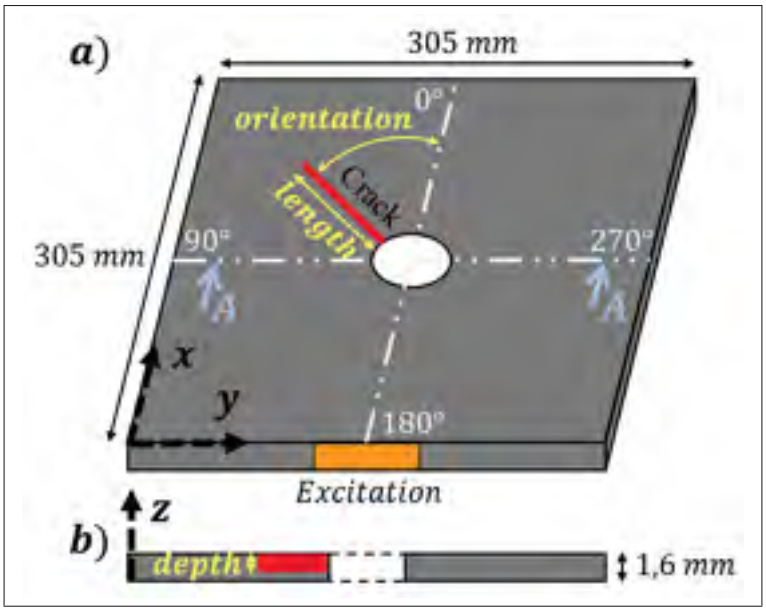

Figure 3.3 Schematic of the structure under study;
a) isometric view and b) Cut A-A view

3.1 Configuration

The configuration concerns the strategy of excitation of the guided waves. The transducer for the guided wave generation was positioned on the thickness of the plate facing the hole. The input signal was a 10-cycle Hann-windowed toneburst centered at 100 kHz with a $1 \cdot 10^{-8} m$ maximum amplitude, and its time representation is given in Figure 3.4. It is applied along the X-axis, defined in Figure 3.3. This input implies that the symmetric fundamental Lamb mode was mostly generated-a fact that can be deduced from the analysis of the mode shape at 100 kHz shown in Figure 3.5, which represents the displacement amplitudes over the thickness. Each mode has a characteristic mode shape at a given frequency, therefore enabling the identification of the propagating modes and their excitability for this configuration.

The mode shapes allows to determine that an out-of-plane displacement according to the plate in Figure 3.3 would generate mostly A_0. Alternatively, an in-plane excitation would mostly generate S_0.

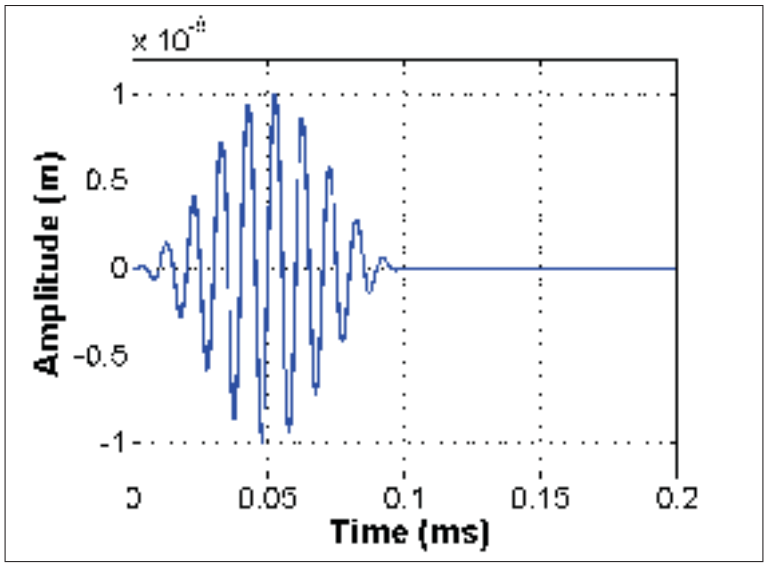

Figure 3.4 Time representation of a 10-cycle Hann-windowed toneburst centered at 100 kHz with a $1 \cdot 10^{-8} m$ amplitude

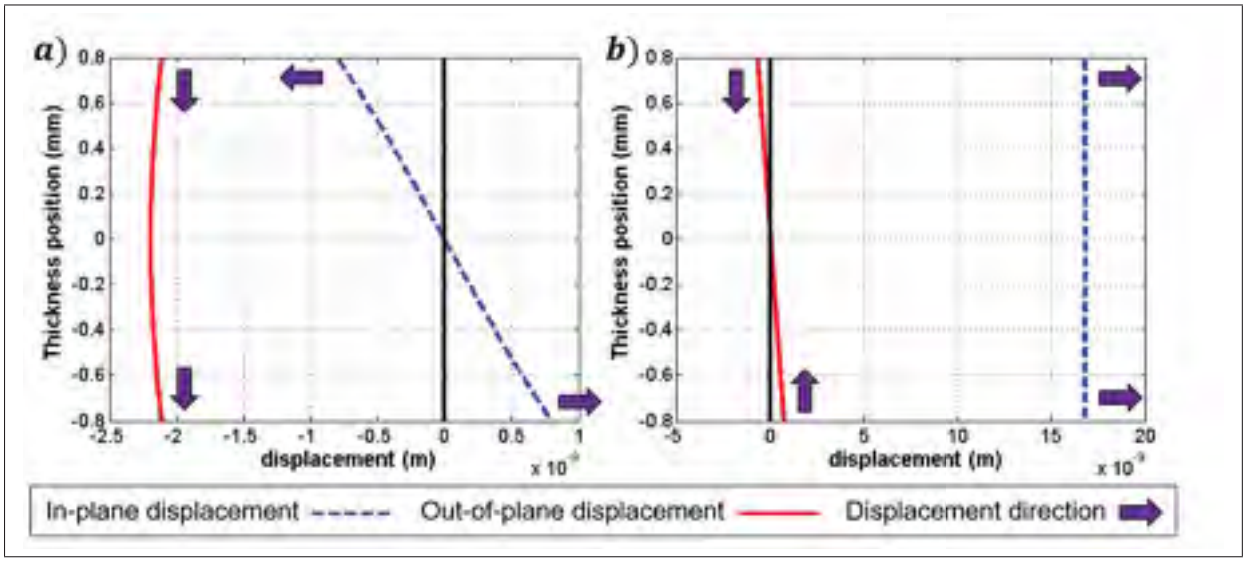

Figure 3.5 Mode shapes for a) A_0 and b) S_0 at 100 kHz

3.2 Methodology

The study was performed on a 305 mm x 305 mm x 1.6 mm alumminum plate with a 4 mm diameter hole at the center of the plate, as schematically presented in Figure 3.3.

The phase velocity dispersion curves extracted from Disperse (developed by Pavlakovic *et al.* (1997)) for a 1.6 mm thick plate are shown in Figure 3.2. Working with guided waves implies multiple modes will propagate, as previously shown in Figure 3.2. Data acquisition and post-processing methodologies were carefully selected in order to study each ultrasonic guided wave mode independently. The measurement points on the structure surface were taken on lines positioned radially around the hole. There were 24 output lines equally distributed around the hole. Each output line result was normalized against the incoming wave amplitude. The baseline signals coming from the simulation of a structure without any crack were then subtracted from the monitoring signals obtained with the simulation of a structure with crack. This procedure was realized at each measuring points.

A two-dimensional fast Fourier transform (developed by Alleyne and Cawley (1991)) was performed on the resulting signals to identify the modes propagating along the line. These representations allowed to differentiate the modes based on their wavenumber. Some examples are shown in Figure 3.6.

Finally, the amplitude of each mode in the 2D FFT was extracted at every output angle in order to plot the mode amplitudes over the output angle, also called the directivity diagrams. The data acquisition and post-processing methods are summarized in Figure 3.7.

The S_0 mode was excited to investigate the crack detection and characterization capabilities.

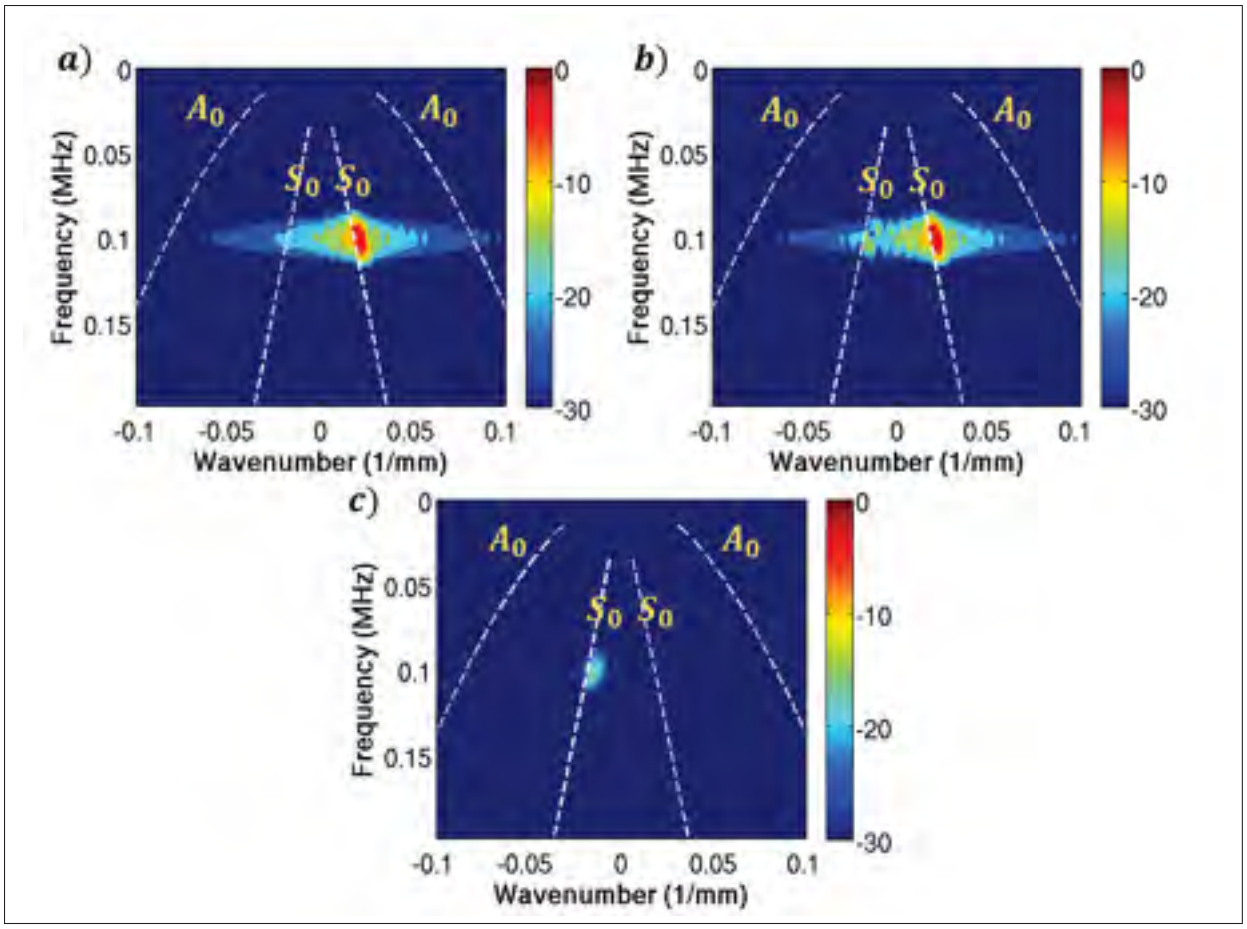

Figure 3.6 Frequency-wavenumber representations of the 180° output angle for a) the defect free model b) model with a 10 mm crack at 90° c) the subtraction between a) and b)

In summary, the scattered field generated by the defect was isolated with a baseline subtraction. A 2D FFT was then performed to differentiate and study the multiple propagating modes.

3.3 Finite element modeling

The finite element simulations were run with Abaqus and Pogo (developed by Huthwaite (2014)). The small size of the model enables the use of Pogo to save time. However, only Abaqus was able to run 3D simulations considering the big amount of memory required.

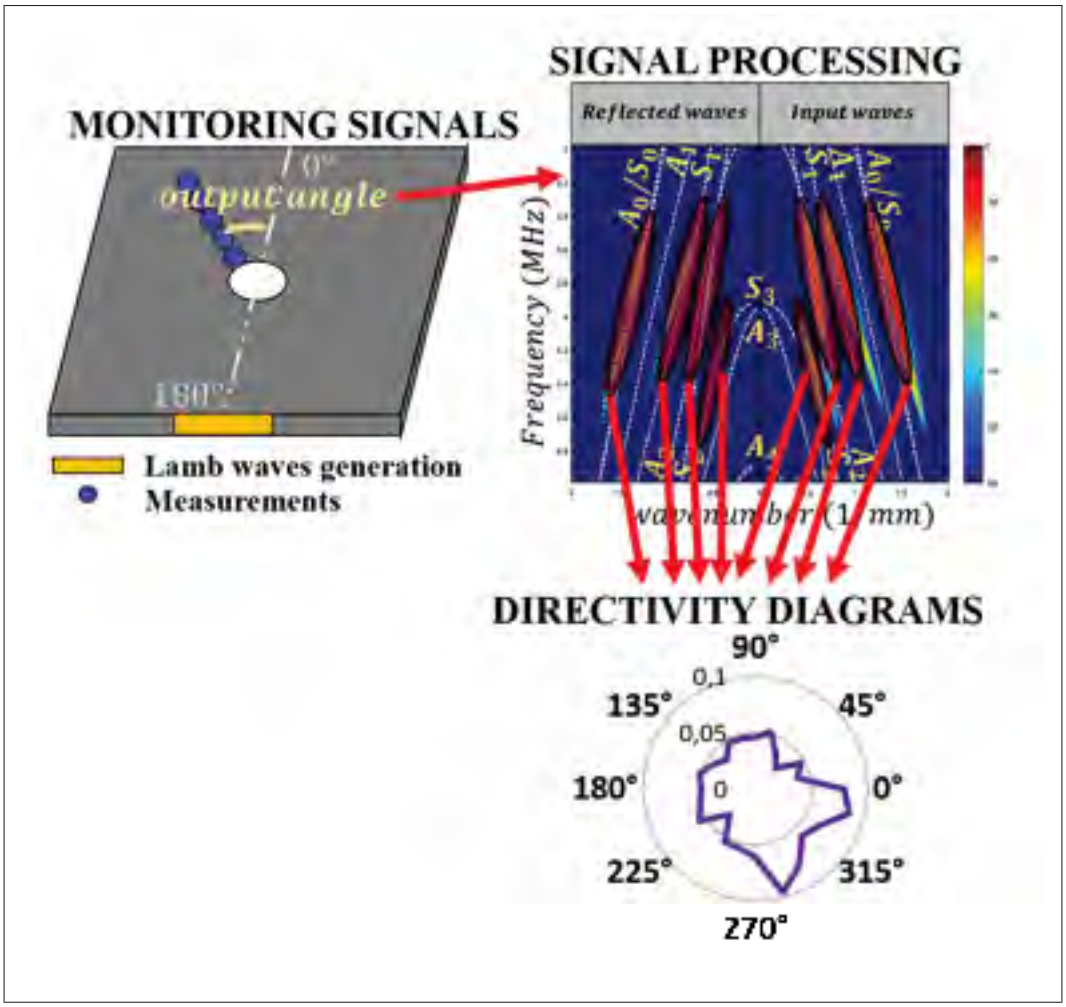

Figure 3.7 Scheme of the SHM method applied in the thesis

As determined in chapter two, 3D 8-node linear brick elements with reduced integration were used in 3-D simulations.

3.3.1 Elements

The frequency components of the input signal are contained in the interval [85 kHz, 115 kHz].

The minimal wavelength determines the element size and is defined by a function of the frequency and the phase velocity: $\lambda = \frac{c_{ph}}{f}$. The minimal wavelength can then be determined using the dispersion curve in Figure 3.8 and the bandwidth of the input signal.

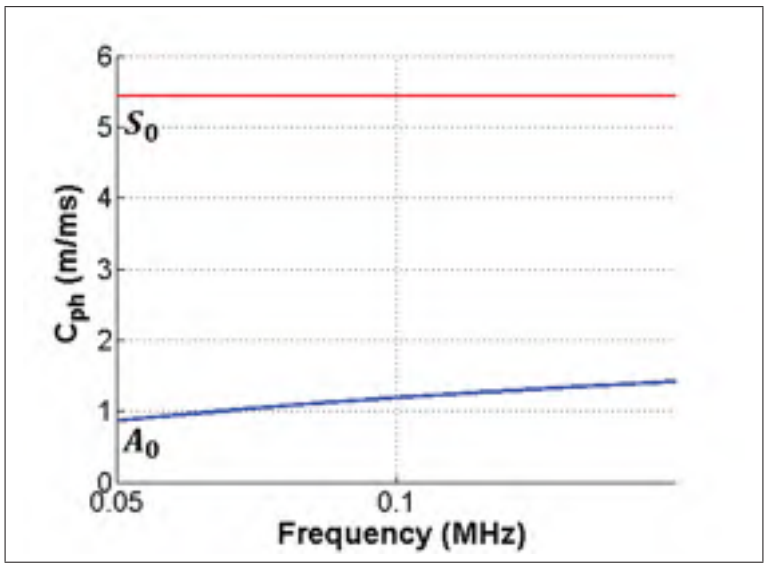

Figure 3.8 Dispersion curves of the Lamb wave phase velocity for a 1.6 mm thick plate

The maximal size of elements chosen must enable accurate results with a reasonable computation time. The A_0 mode governs the element size, as it has a smaller wavelength than S_0 at low frequency. The minimal wavelength value in the signal is 10.8 mm for A_0 and 44.2 mm for S_0; the results are summarized in Table 3.1. To combine minimal computation time with usable results the maximal element size was 1 mm according to Drozdz (2008).

3.3.2 Absorbing regions

In order to avoid multiple reflections from the boundaries of the model, an unbounded structure is approximated by the use of absorbing layers. These layers are an important

Table 3.1 Wavelength of the different mode for the extreme and the central frequencies for a 10-cycles Hann-windowed signal centered at 100 kHz

Mode \ **Frequency**	**85 kHz**	**100 kHz**	**115 kHz**
A_0	13.1 mm	11.5 mm	10.8 mm
S_0	62.1 mm	53.1 mm	44.2 mm

part of the model because they improve the quality of the measured signals. If the absorbing region is efficient, then the effect of the cracks on the received signal is not denatured with reflections coming from the structure boundaries. In addition, the interpretation of the results is easier. Determining the values that define the absorbing region is critical for having reflections from the edges remain as low as possible in the signals.

The number of absorbing layers selected for the low frequency simulations was 100. The width of a layer was 1 mm, which corresponds to the mesh size. These choices allow a good absorption of incident waves.

The damping α characterizes the layers. It follows a mathematical law defined by Drozdz (2008) by the Equation 3.1

$$\alpha = K \left(\frac{m}{N} \right)^p \tag{3.1}$$

Where $K = 8 \cdot 10^6$, m is the number of the layer varying from 1, for the closest layer to the actual study part, to N, on the edge of the model and $p = 3$. The evolution of the damping value in absorbing layers is represented in Figure 3.9. These parameters were determined by iteration, and the chosen values provided the best results.

The final model is shown in Figure 3.10.

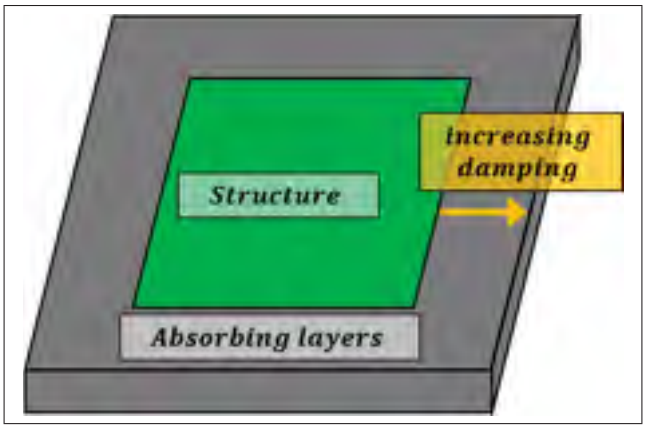

Figure 3.9 Evolution of the damping value in the absorbing layers; the structure under study is in green and the absorbing region in gray

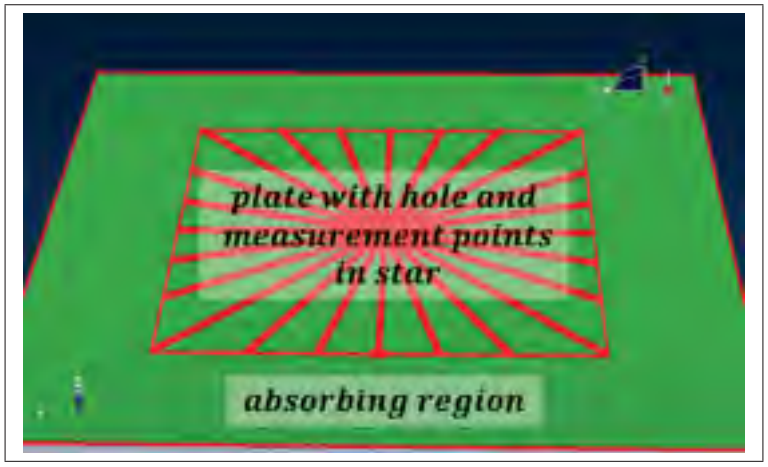

Figure 3.10 Screenshot of the model from ABAQUS

3.3.3 Model validation

The FE model built as described in this section had to be validated in order to certify the results extracted from these simulations. To this end, the *simulated signal* module of the software Disperse was used to extract the theoretical form of the propagated signals. The properties of the input signal that were considered are: the central frequency, type of window and cycle number. The signals extracted from Disperse were then

compared to the finite element simulations results. The signals were captured before the interaction with the hole or the defect.

Six propagation distances were considered: 25 mm, 50 mm, 75 mm, 100 mm, 125 mm and 140 mm. Examples of comparisons between finite element simulations and theoretical signals are shown in Figure 3.11. Due to the in-plane excitation, the S_0 mode is mostly generated. The validation is therefore achieved with this mode.

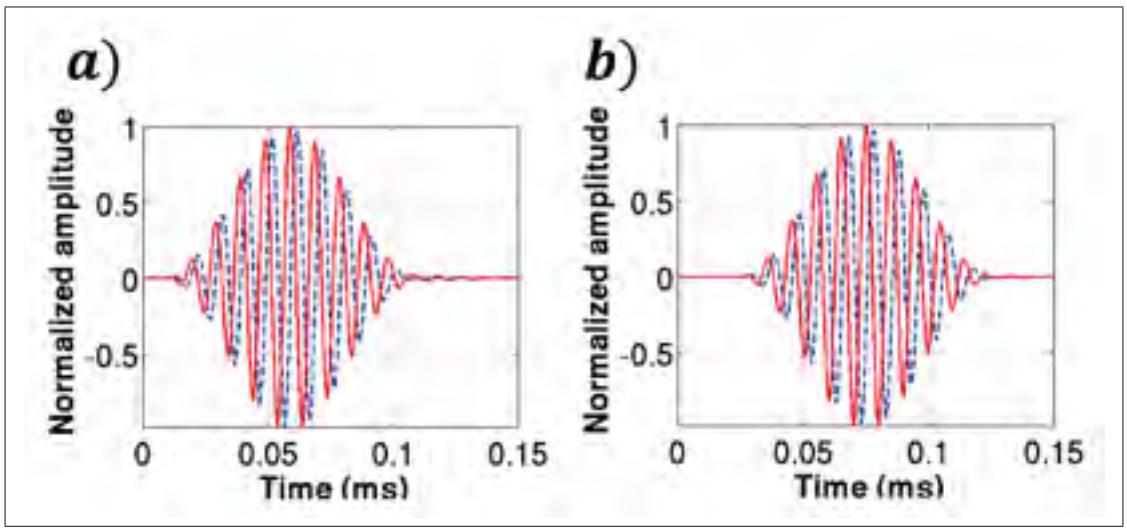

Figure 3.11 10-cycle Hann-windowed toneburst in-plane excitation at 100 kHz after a propagation of a) 50 mm and b) 140 mm; the dashed line is the theory and the plain line is the finite element simulation results

There were differences in time of arrival and amplitude for all of the cases as shown in Figure 3.11. The time delay between simulations and disperse signals was constant over the propagation length, estimated to be 0.003 ms. This means that this delay was not introduced by the finite element parameters, for otherwise the delay would have increased with the number of elements crossed by the signal. Thus, this phenomenon was removed from the simulation results by shifting the simulation signal times of arrival 0.003 ms ahead.

Without the time delay, the amplitude of each point on the curves can be compared in order to determine the similarity of the signals. For each propagation distance, a correlation between the signals from Abaqus and the theory from Disperse was performed; these results are presented in Table 3.2.

Table 3.2 Correlation between signal propagation extracted from Disperse and finite element simulation

Distance	25 mm	50 mm	75 mm	100 mm	125 mm	140 mm
Correlation coefficient	0.9715	0.9742	0.9765	0.9765	0.9713	0.9860

The average correlation coefficient is 0.976, which means that the results from simulations differed by 2.4% in amplitude from the theory.

In addition, the waves seem not to be dispersive. This phenomenon comes from the low dispersion at this frequency as shown in Figure 3.8. Around 100 kHz the slope of the S_0 phase velocity dispersion is low, which means that the dispersion effect is low in this frequency region for S_0 and that the signals stay nearly the same as the original excitation wave.

Overall, the values of time delay and of differences in amplitude were negligible. Consequently, the model was validated.

3.4 Finite element parametric study

The finite element parametric study was achieved with the model validated above. The objective is to determine the effect of the crack parameters on the signal in order to find technique for crack detection and monitoring with low frequency guided waves.

3.4.1 Crack orientation effect

Simulations of many crack orientations were run in order to analyze the capabilities of crack detection and orientation determination with S_0 at low frequency. The crack orientations varied from 0° to 315° with a 45° angle step. The model is represented in Figure 3.12. Cracks were through-thickness and 3 mm long for all the models.

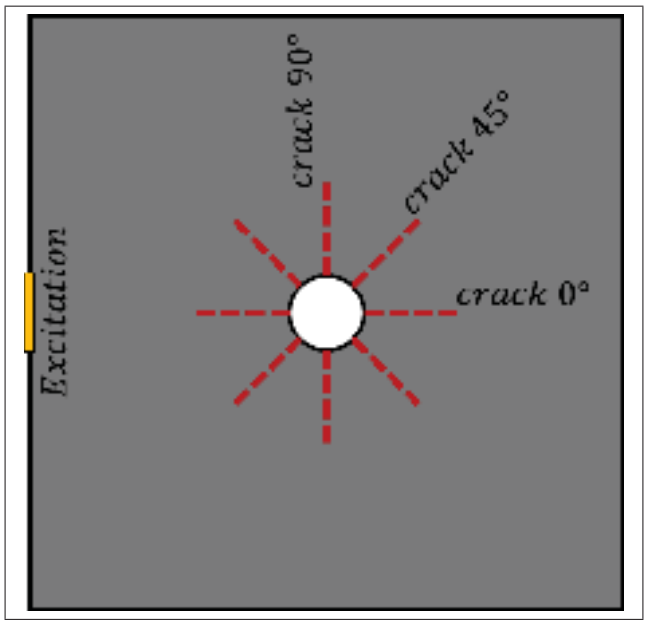

Figure 3.12 Crack orientations for the determination of orientation effects on the signals

The effects of the cracks on the signals were then isolated by using a baseline subtraction approach. The directivity diagrams of S_0 were plotted to find patterns for the orientation determination. The directivity diagrams for S_0 with through-thickness 3 mm cracks at different orientations are shown in Figure 3.13.

The crack orientation had an influence on the form of the diagrams. The most likely symmetry axis of each figure corresponds to the axis on which the crack is

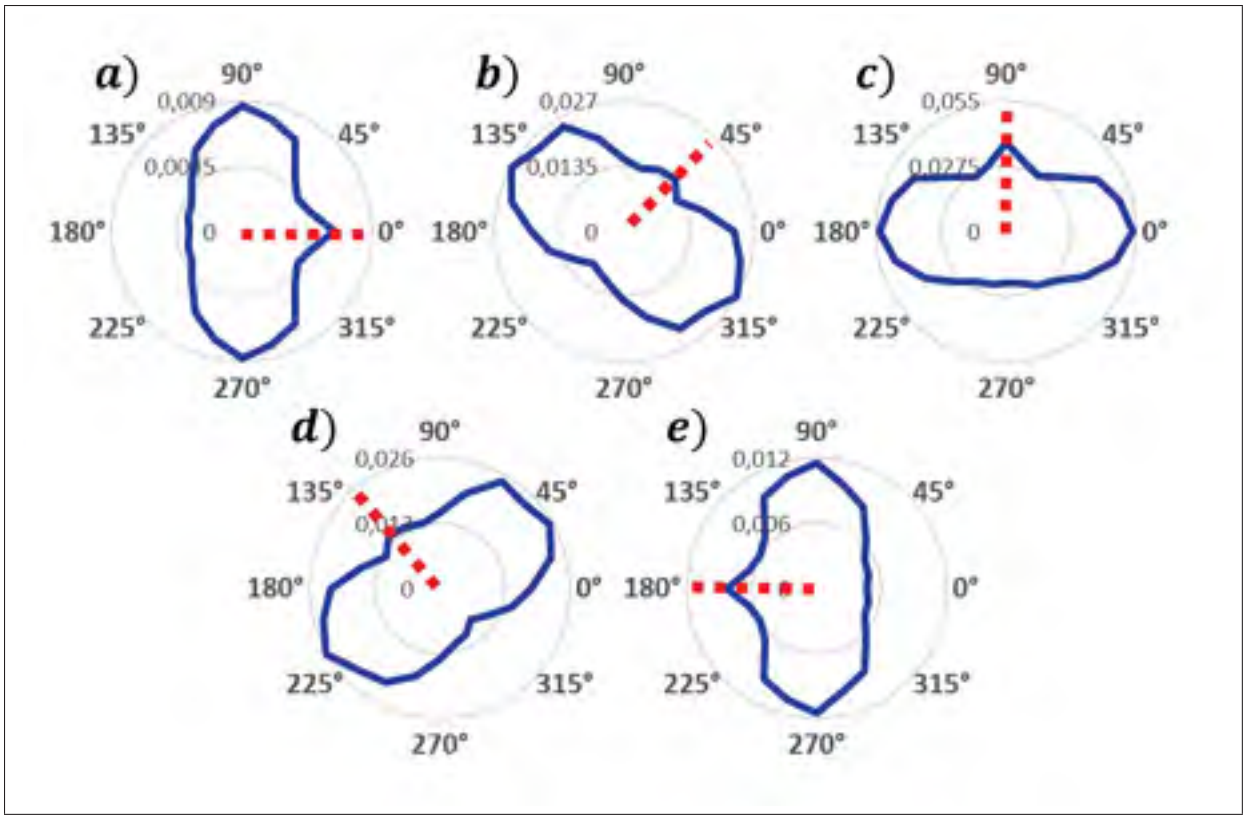

Figure 3.13 S_0 directivity diagrams coming from 3 mm long through-thickness cracks at different orientations; the crack positions are represented by a red dashed line

positioned. The precise orientation cannot be determined with a universal procedure. The method of the symmetry axis enables to determine the orientation modulo 180°, and thus it could be α or $\alpha + 180°$.

Knowing the axis is sufficient to have all of the relevant monitoring information concerning the orientation. It allows the calculation of the solicitations applied to the crack, as they are the same whether the orientation is α or $\alpha + 180°$.

3.4.2 Crack length effect

The influence of the length on the backscattered waves was investigated by varying the length parameter illustrated in Figure 3.3. The considered lengths varied from 0.5 mm to 15 mm. All the cracks were through-thickness and oriented at 90°. The baseline subtraction technique is also used here to plot S_0 directivity diagrams.

The purpose of this section is to find a way to determine the length of cracks by interpreting the backscattered waves they generated. Some of the directivity diagrams of backscattered S_0 are shown in Figure 3.14.

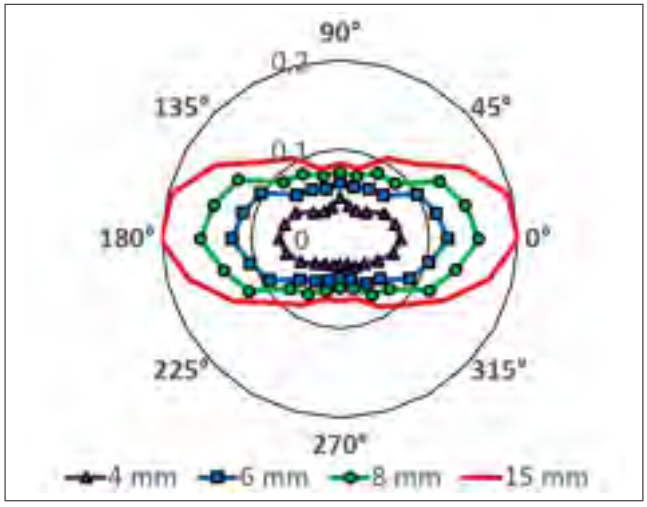

Figure 3.14 S_0 amplitude directivity diagrams for different crack lengths

The directivity diagrams showed a coherent evolution of the amplitudes over the crack length for the S_0 mode reflected by the crack. The longer the crack was, the higher the average amplitude of S_0 was, as is shown in Figure 3.14. To be able to determine the length of a crack with S_0, a curve linking the crack length to the S_0 amplitude is necessary.

To determine the crack length with only the S_0 amplitude, its evolution has to be monotonic in order to match every amplitude value with a unique crack length value. Only the 0°, 60°, 150° and 210° output lines were analyzed here to reduce the amount of curves; though theoretically the other output angles could be used as well.

The S_0 amplitudes studied are plotted over the crack length in Figure 3.15. The global trends of all of the curves are the same, but the values are different.

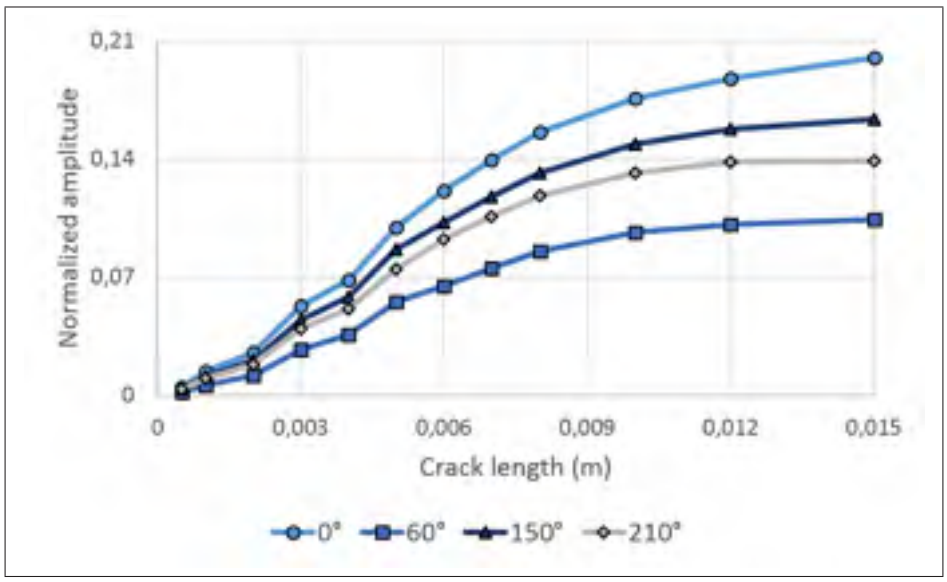

Figure 3.15 S_0 amplitude values over the crack length for different output line angles

The evolution of the S_0 amplitude over the crack length enables the monitoring of the crack length. The method consists of comparing a value of amplitude extracted from a monitored structure with the corresponding value of crack length on the standard curve obtained from simulations. This would enable to approximate the length of the crack and thus plan the maintenance.

This procedure is reproducible for any crack orientation. In conclusion, the length of any crack is sizable through analysis of only one output angle.

3.5 Discussion about crack detection using low frequency guided waves

This section showed that a crack can be monitored with the low frequency fundamental Lamb modes using the proposed configuration and methodology. The length and the orientation of the crack can be determined with the S_0 directivity diagrams and S_0 amplitudes using the methods presented in this chapter.

The study of different crack lengths enabled the determination of the detection limit in this configuration. A 3 mm long crack oriented at 90° was detected with an amplitude of S_0 25.46 dB below the incident wave, whereas a 2 mm crack oriented at 90° was detected with an amplitude 31.84 dB below the incident wave. This means that, with a detection threshold 30 dB below the amplitude of the incident wave, the detection limit of S_0 at 100 kHz in this structure for a crack oriented at 90° is between 2 mm and 3 mm. The detection threshold was determined by the experimental setup used high frequency guided wave experiments.

Since the FE model had two elements in the thickness, only through-thickness, or half-through-thickness cracks were studied. This provided an insufficient amount of data to study the depth effect.

The A_0 mode at 100 kHz has a smaller wavelength than S_0; therefore it would in principle enable detection of smaller cracks. The study of antisymmetric modes was not conducted in this thesis because its main objective is to present a comparison between low and high frequency capabilities in crack detection. The same methodology could be used for the study of antisymmetric modes.

CHAPTER 4

HIGH FREQUENCY LAMB WAVES CAPABILITIES FOR CRACK CHARACTERIZATION

The detection limit for low frequency guided waves was between 2 mm and 3 mm for a crack oriented at 90° as determined in the previous chapter. In this chapter, the high order modes of guided waves at high frequency are investigated to evaluate the advantages and disadvantages they present in crack detection and monitoring as compared to low frequency guided waves.

The aim of this section is to study the capability of high order guided wave modes to detect crack and characterize cracks from a point as early as the crack initiation. The advantage provided by high frequency excitation concerning the crack length detection limit is investigated, as well as the influence of the crack parameters defined in Figure 3.3.

Simulations with excitation at 100 kHz and 4 MHz along the X-axis (previously defined in Figure 3.3) were run to compare the performance of each central frequency in the detection of a through-thickness crack oriented at 90°. In both cases, the excitation signal was a 10-cycle Hann-windowed toneburst centered at either 100 kHz or 4 MHz.

The configuration of the high frequency guided wave study was therefore identical to the low frequency one, except for the fact that the central frequency of the excitation was 4 MHz in this section. The monitored plate dimensions were unchanged.

The FE parameters were the same as those defined in Chapter two. A ratio of number of elements per wavelength between 10 and 20 was applied to the models and the time increment was defined to ensure stability of simulations. The methodology to determine the crack parameters with the propagating modes was the same as in the

previous chapter. The parameters studied in this chapter are the crack orientation, length and depth as previously defined in Figure 3.3.

4.1 Finite element modeling

The finite element modeling was performed using the Abaqus finite element simulation package detailed by Simulia (2013). The explicit scheme was used to solve the elasto dynamic equations governing the propagation of elastic waves. In order to have accurate results from finite element simulations some parameters such as the element size and the time step must be carefully selected. The elements used in the models were linear brick elements with reduced integration; they were used because of their ease of implementation with regular geometries and therefore provided a good approximation of the real structure.

4.1.1 Model reduction

In 3D, the model rapidly increases in size and the computation times rapidly become unreasonable. In this study, the modeling domain was reduced to its minimum. The approach consisted of keeping two zones of the actual structure as presented in Figure 4.1. The first zone is the propagation area where the excitation only propagates without interaction with structural features. This region was two elements wider than the transducer size. The second zone monitors the wave scattered from the hole and the crack, and is a square region of 50 mm on each side. These dimensions govern the resolution on the wavenumber axis in the frequency-wavenumber representations. The selected value enabled sufficient resolution to differentiate the modes in the 2D FFT. The model volume was reduced by 90% with negligible effect on the results.

The thickness of the plate is a parameter that defines the dispersion curves. Therefore, the value of this parameter was unchanged here to keep the same dispersion effects.

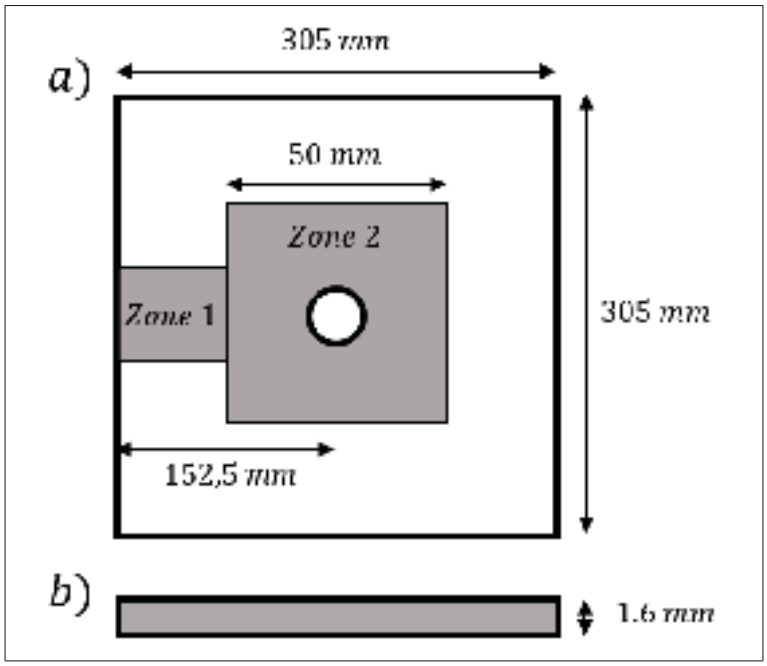

Figure 4.1 Dimensions of the plate and the reduced model (gray); a) top view and b) front view

In order to limit the number of reflections, an unbounded plate was approximated using Absorbing Layers with Increasing Damping (ALID) as done in Chapter 3.

4.1.2 Elements

The types of elements implemented in the high frequency models were the same as in the low frequency simulations. However, their size is different because the frequency of excitation is higher. The element size applied in the high frequency models was 0.1 mm. This value enables to have the ratios of number of elements per wavelength given in Table 4.1 considering that the range of frequency components in the signal is $[3.5\ MHz,\ 4.5\ MHz]$. Therefore the modes able to propagate in the structure are the modes for which order is up to three as shown previously in Figure 3.2.

According to Drozdz (2008), the maximum error value was 3.5% made on the velocity of fundamental modes.

Table 4.1 Ratio of number of elements per wavelength for the different modes for the extreme and the central frequencies for a 10-cycles Hann-windowed signal centered at 4 MHz kHz

Mode	**Wavelength**	**Elements/λ**
A_0	0.65-0.829 mm	6-8
S_0	0.65-0.845 mm	6-8
A_1	0.746-1.05 mm	7-10
S_1	0.914-1.49 mm	9-14
A_2	1.21-1.95 mm	12-19
S_2	1.41-2.10 mm	14-21
A_3	$\geq$ 2.6 mm	$\geq$ 26
S_3	$\geq$ 1.81 mm	$\geq$ 18

4.2 Model validation against experiment

The simulation and experiment results for a plate without cracks are compared to validate the FE model.

4.2.1 Setup

The experiments were carried out on a 305 mm x 305 mm x 1.6 mm plate, with a 4 mm diameter hole in its center as defined in the previous chapter in Figure 3.3. The Lamb waves were generated by a piezoelectric longitudinal transducer with an out-of-plane polarization; its central frequency was 5 MHz. The transducer was bonded on the side of the plate.

The detection was performed using a laser Doppler vibrometer, which enables to perform non-contact measurements. The laser is directed toward the surface that is being examined, and the vibration and frequency are extracted from the Doppler effect extracted from the laser reflections from the surface movement. The average signal-to-noise ratio of this laser was approximately 32 dB; thus, only amplitudes above this limit were considered in the simulations. The measurements were taken on the

plate surface on lines positioned radially around the hole; there were 24 output lines equally distributed around the hole. The results of every output line were normalized against the incoming wave amplitude. The length of every line was 120 mm. This value differs from the simulations but it results in a better resolution on the wavenumber axis. Pictures of the setup are shown in Figure 4.2 for illustration.

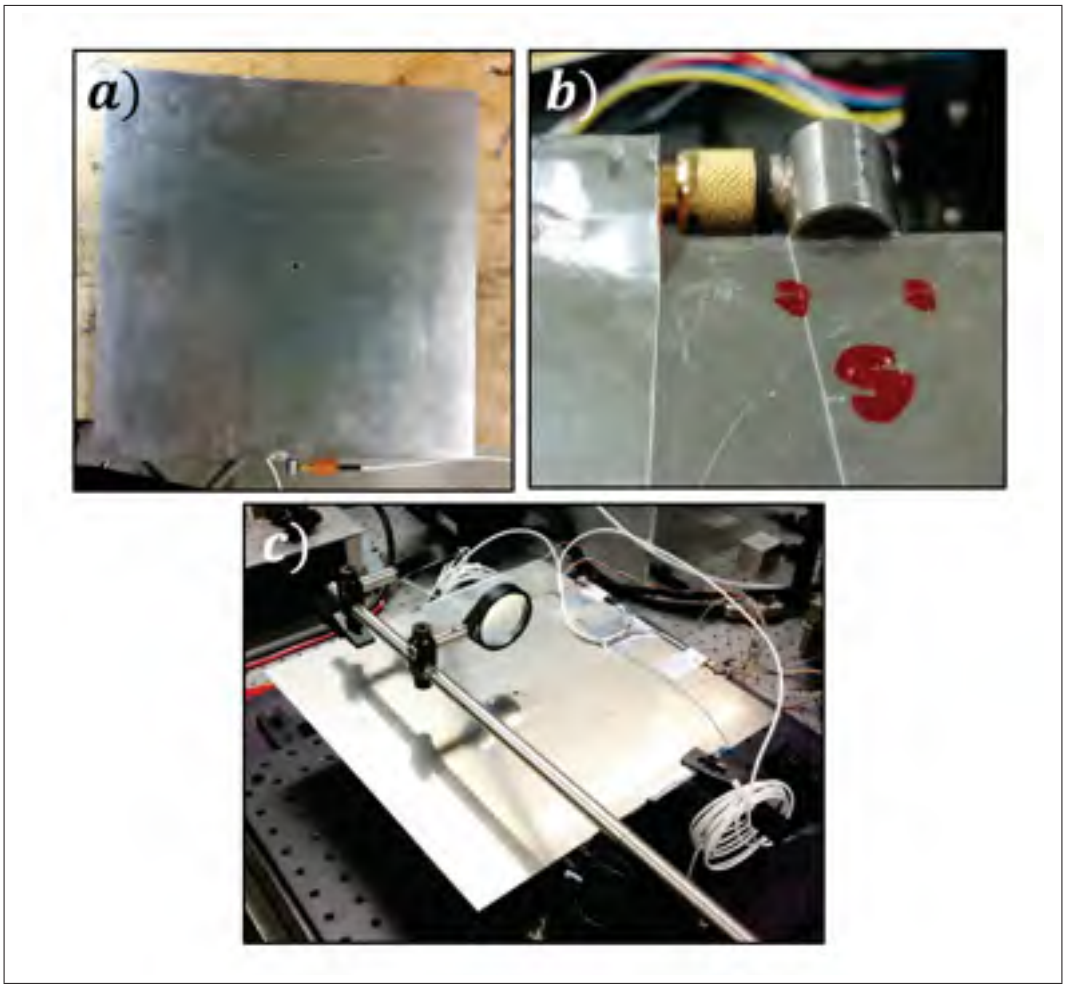

Figure 4.2 Experimental setup: a) picture of the plate and the transducer bonded to the side of the plate; b) zoomed image of the transducer; c) plate installation for laser detection

4.2.2 Results

In order to validate the model, the frequency-wavenumber representations of the experimental data and the simulations were compared.

The directivity diagrams of the incident and the reflected modes were considered in the simulation of the studied structure without defects. Figures 4.3 and 4.4 show the comparison between simulation and experimental directivities for each symmetric mode for the incident (Figure 4.3) and the backscattered (Figure 4.4) waves.

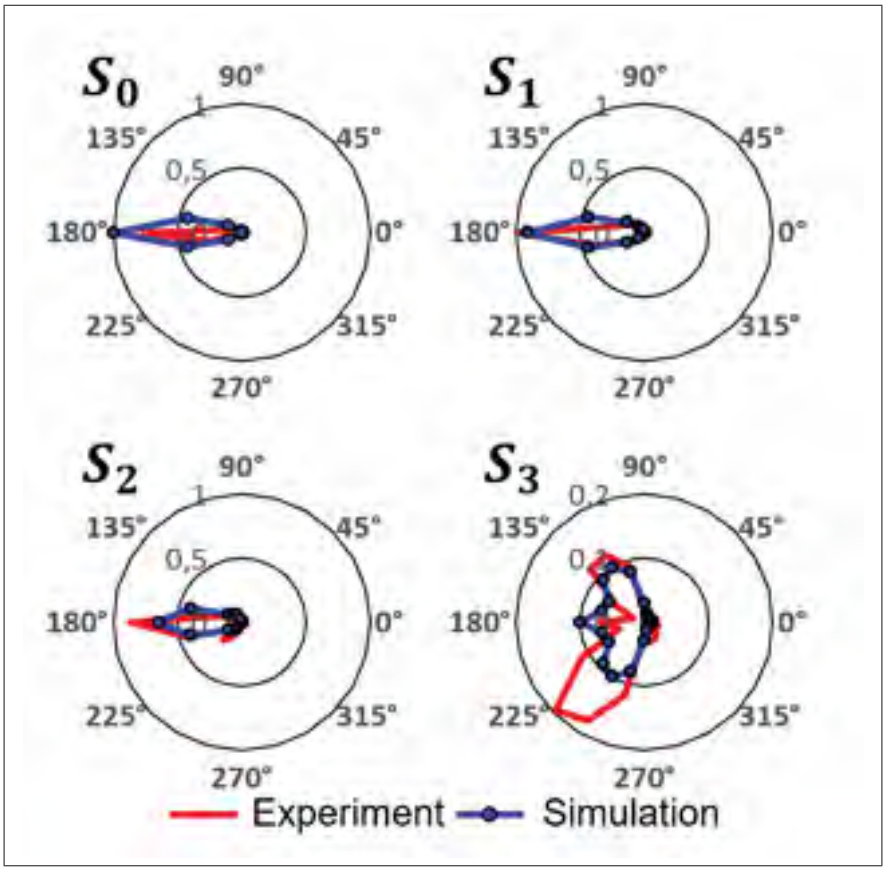

Figure 4.3 Directivity diagrams of incident symmetric modes for a defect-free plate

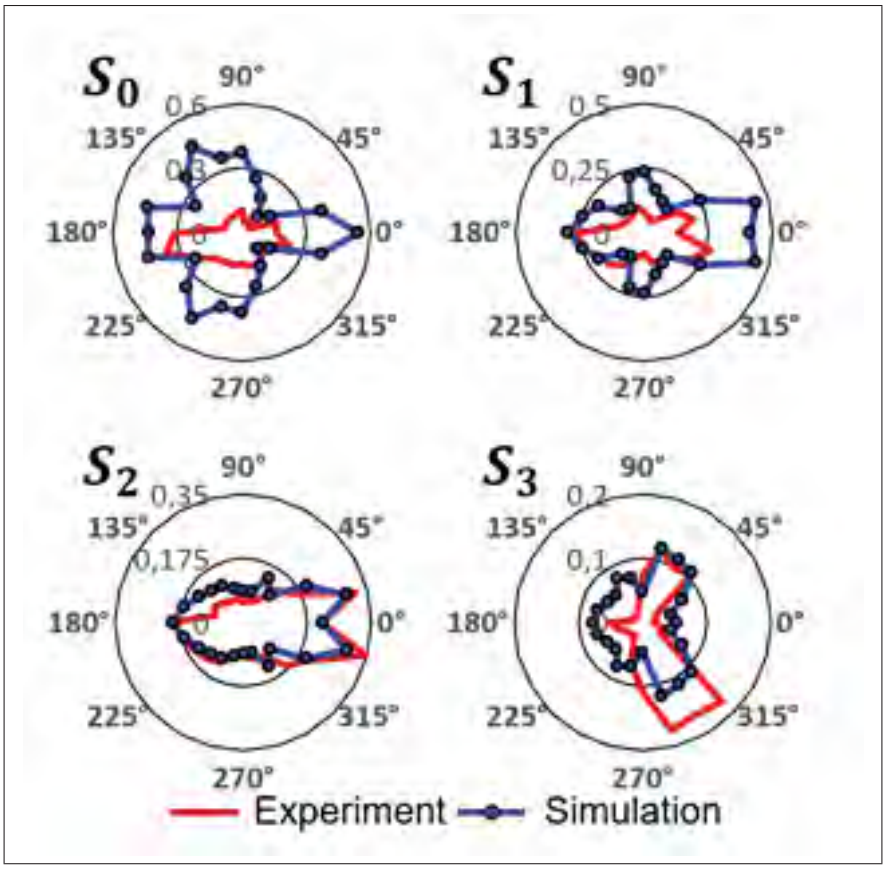

Figure 4.4 Directivity diagrams of backscattered symmetric modes for a defect free plate

Noticeably, each mode that propagated in the simulations also propagated in the experiments. Moreover, the figures of mode directivity from simulations are similar to experimental ones; though there were some amplitude differences. The local maximum and minimum are on the same angle, however.

For the incident modes S_0, S_1 and S_2 the energy is concentrated on the 180° angle, which is the direction from which the excitation came; and the width of the directivity diagram is similar in experiment and simulation. The directivity diagram of the S3 mode has the same shape in experiment and simulation. The maximum values are on the same angles or on adjacent angles.

The reflected modes S_0 and S_1 have the same shape in experiment and simulation but the amplitudes in experiment are lower. The reflected S_2 and S_3 directivities from the simulation are close to the experimental results. They present the same local maximum orientations and the values are similar. The difference is thought to be because of the number of elements per wavelength, which is different for every mode. This ratio increases with the mode order; S_0 has the smallest ratio and S_3 the greatest.

The attenuation was not considered in the simulations. Although the attenuation in aluminum is low, this could lead to lower amplitudes in the experiments as compared to in the simulations. The model without cracks for high frequency guided wave propagation is thus validated.

4.3 Comparison between the low and high frequency detection capabilities

To achieve the detection of very small cracks, the wavelengths have to be as small as possible. For this purpose the frequency was increased to shorten the wavelength. The comparison of the low and high frequency performances was made with excitation signals centered at 100 kHz and 4 MHz.

The results of the simulations of crack detection in the investigated structure are shown in Table 4.2 for the S_0 and S_1 modes respectively. The tables show that at low frequency, the backscattered signal of S_0 coming from a 2 mm long crack after baseline subtraction is more than 30 dB below the incident amplitude. With a 4 MHz excitation signal, a 0.1 mm long crack can be detected with an amplitude only 23 dB below the incident amplitude. The S_0 mode at 100 kHz was studied in the previous chapter.
Therefore, in order to monitor crack from the point of initiation in a safety critical component, the use of high frequency guided wave should be favored. These results were presented at the 2015 Review of Progress in Quantitative Nondestructuve Testing and will be published in the conference proceedings.

Table 4.2 Comparison of backscattering coefficients at low and high frequencies for different crack length

Crack length	**Mode**	**Max reflection coeff.**
3 mm	S_0 at 100 kHz	-25.46 dB
	S_1 at 4 MHz	-7.23 dB
2 mm	S_0 at 100 kHz	-31.84 dB
	S_1 at 4 MHz	-6.79 dB
1 mm	S_0 at 100 kHz	-37.08 dB
	S_1 at 4 MHz	-8.76 dB
0.1 mm	S_0 at 100 kHz	-
	S_1 at 4 MHz	-23.44 dB

4.4 Finite element parametric study

As the model has been validated, we are able to achieve a finite element parametric study on the capabilities of high frequency Lamb waves to detect and size a crack on the circumference of a through-thickness hole with finite element simulations. The interaction of guided waves with defects has already been studied in the literature by Lowe *et al.* (1998); Ghosh *et al.* (1998); Staszewski *et al.* (2007); Tua *et al.* (2004), but the results are specific to the structure, the frequency, the modes used and the defects. This section presents the influence of the crack parameters on the backscattered signals from the defect.

4.4.1 Crack orientation effect

The capability of high order Lamb modes to determine the crack orientation with an SHM approach was investigated. Five different orientations were considered, varying from 180° to 360° with a 45° step. The frequency-wavenumber representations of the signals after baseline subtraction were plotted and the directivity diagrams were extracted from them.

After analysis of the diagrams of backscattered symmetric modes, S_2 appeared to be the most sensitive to orientation changes, and thus the most effective to determine

this parameter. All of the amplitudes were normalized against the incident energy, as defined earlier as the maximum displacement amplitude on the 180° output angle.

The relevant diagrams are presented in Figure 4.5. As shown by the results, the most likely symmetry axis of the figures is the axis on which the crack is. With this observation, the crack axis could be defined, but there was no universal procedure to determine the orientation. This axis gave the crack orientation modulo 180°. However, these two cases are symmetric with respect to the center of the hole. Thus, whether the orientation is α or $\alpha + 180°$, the structure has the same mechanical behaviour, regardless of the solicitation direction. This means that the critical crack size would be the same for both cases, and as a result knowing the crack axis, length and depth would be enough to allow a decision to be made on the maintenance required.

4.4.2 Crack length effect

The lengths of the cracks used to study the influence of this parameter on the backscattered signals are: 0.1 mm, 0.2 mm, 0.3 mm, 0.4 mm, 0.5 mm, 1 mm, 1.5 mm, 2 mm and 3 mm. The mode that was most sensitive to the changes in the crack length was S_1. This is convenient because S_1 has the smallest wavelength among the high-order symmetric modes excited with the proposed setup. The S_1 amplitude increased over the crack length; the longer the crack, the higher the average amplitude of S_1 around the hole was, as shown in Figure 4.6.

However, to be able to monitor the evolution of the crack length, the evolution of the amplitude must be monotonic. Here, the 15° and 165° output angles were used, and the S_1 amplitudes curves over the crack length at these angles had a monotonic evolution and are shown in Figure 4.7.

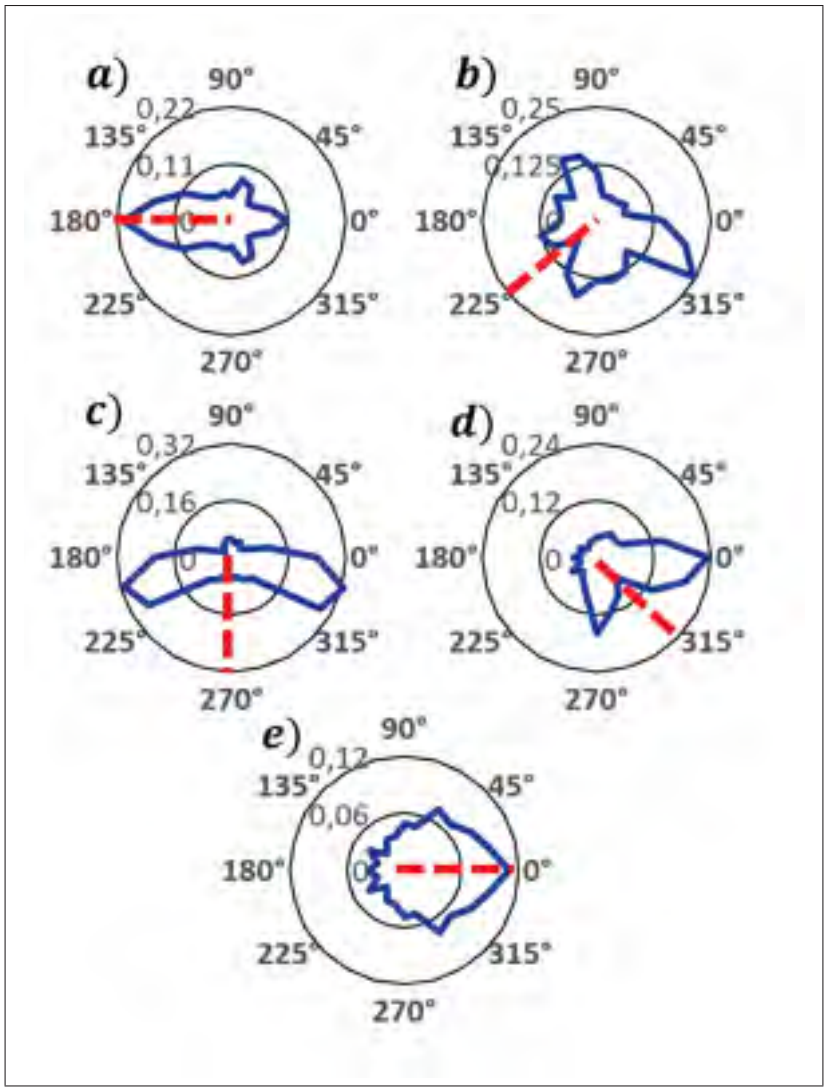

Figure 4.5 Directivity diagrams of S_2 for cracks at a) 180°, b) 225°, c) 270°, d) 315° and e) 360°; the dashed lines represent the crack positions

The crack length can therefore be determined by matching the S_1 amplitude with the crack length using a standard curve. The output line angles must be the same for the amplitude measure and the standard curve.

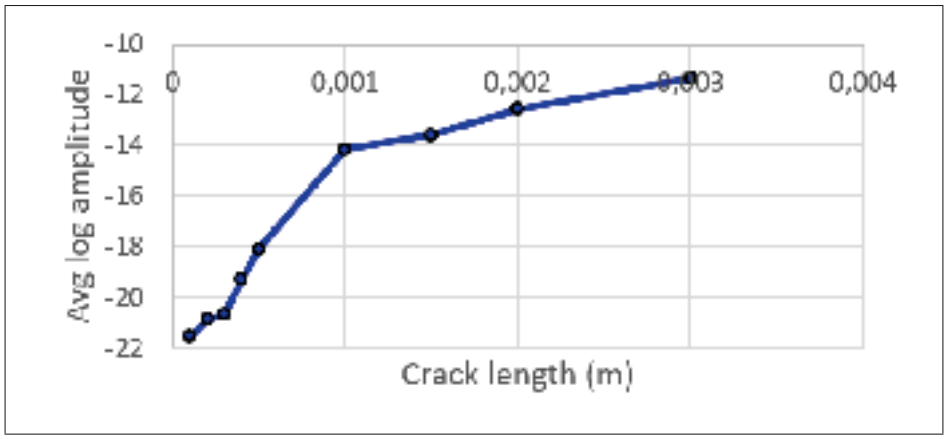

Figure 4.6 S_1 average amplitude over the crack length

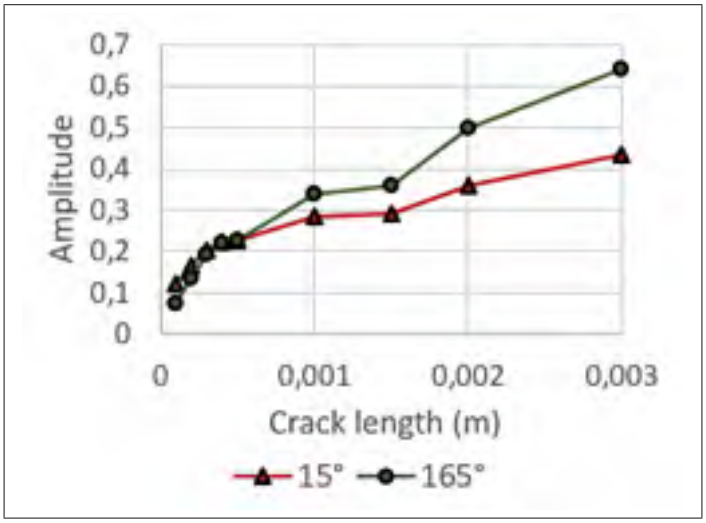

Figure 4.7 S_1 amplitude for the 15° and 165° output lines over the crack length

4.4.3 Crack depth effect

The depth of a crack is a critical monitoring parameter for SHM systems. To investigate the ability of high-order modes to size the depth of cracks, simulations were run with a crack length of 3 mm, an orientation of 90°, and a depth varying from 25% to 80%. The fact that the crack is part through-thickness causes the damage to become asymmetric with respect to the middle plane of the plate. The model asymmetry generated antisymmetric modes. As shown in Figure 4.8, all the antisymmetric modes

up to 3rd order appeared in the frequency-wavenumber representations, whereas only symmetric modes were backscattered by a through-thickness crack.

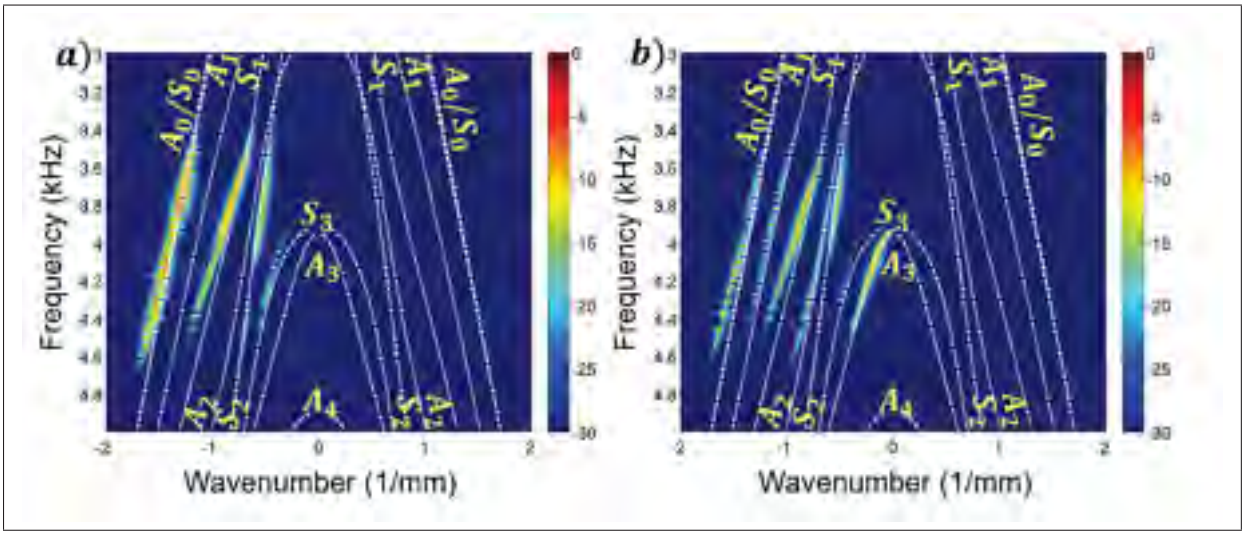

Figure 4.8 Frequency-wavenumber representations of the 165° output line extracted from the simulation of a) 3 mm long through-thickness crack and b) a 3 mm long half-through-thickness crack, both oriented at 90°

In the case of the depth, all of the propagating modes had a non-monotonic evolution, and as a result, the depth is not sizable using the approach used with the crack length. Some examples of the evolution of the A_3 amplitude over the crack depth are shown in Figure 4.9 c). However, with a symmetric excitation, the presence of antisymmetric modes in the wave field scattered from the crack indicates that the crack depth is part through-thickness.

The interactions of high frequency guided waves with part through-thickness cracks are similar to the interactions between low frequency guided waves and notches at different depths as proved by Alleyne and Cawley (1992); Mckeon *et al.* (2012).

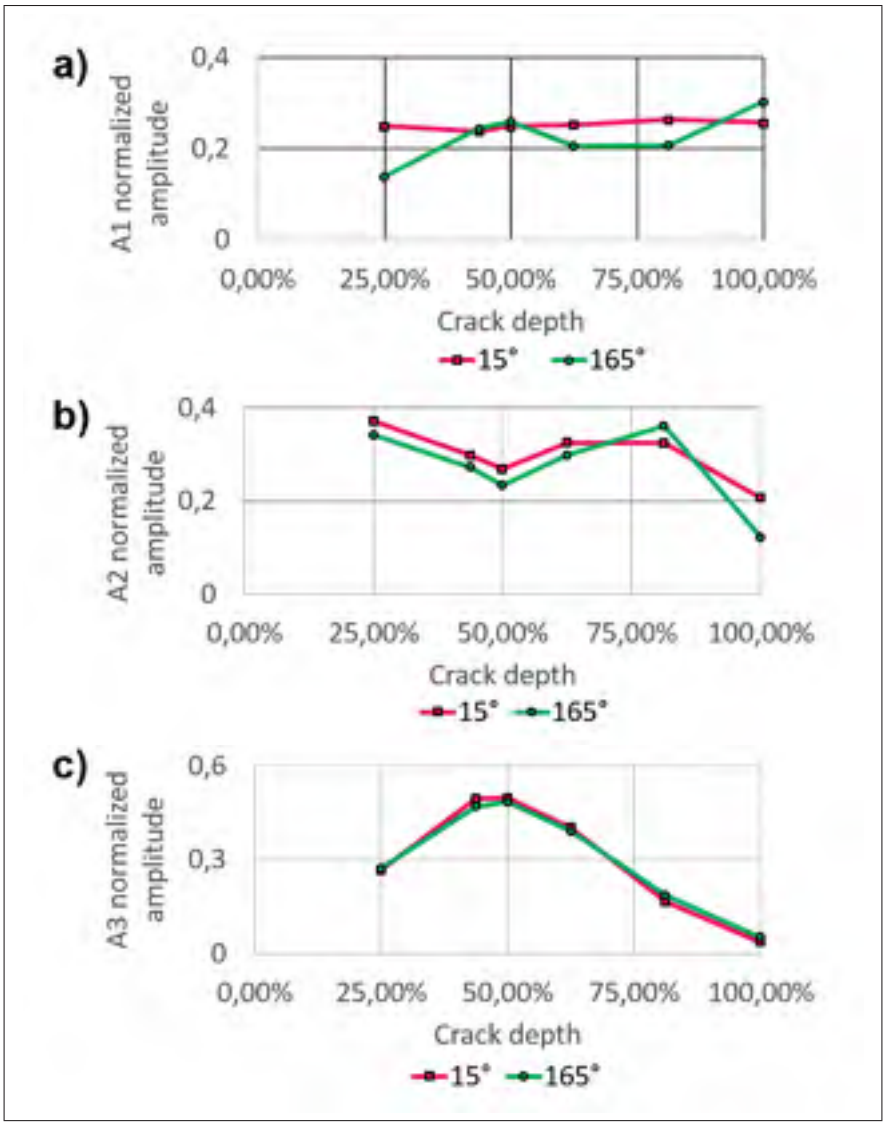

Figure 4.9 A_1, A_2 and A_3 amplitudes for the 15° and 165° output lines

The evolution of the A_3 maximum amplitude over the crack depth can be explained by analyzing the shapes of the incident modes, in particular S_2. Assuming that the crack is open, when the excitation wave hits the first crack surface, the wave is reflected on the depth of the crack and transmitted on the rest of the plate thickness. By using the mode shape of A_3 and comparing it to the incident mode shapes, it appears that the out-of-plane shapes of S_2 and A_3 are similar. For a depth comprised between 0% and 50% of the plate thickness, the shapes of the out-of-plane displacement of A_3

is the same than the S_2 with a phase reversal; for a depth between 50% and 100% the shapes of the out-of-plane displacement are similar without any phase changes. The modes shapes are shown in Figure 4.10.

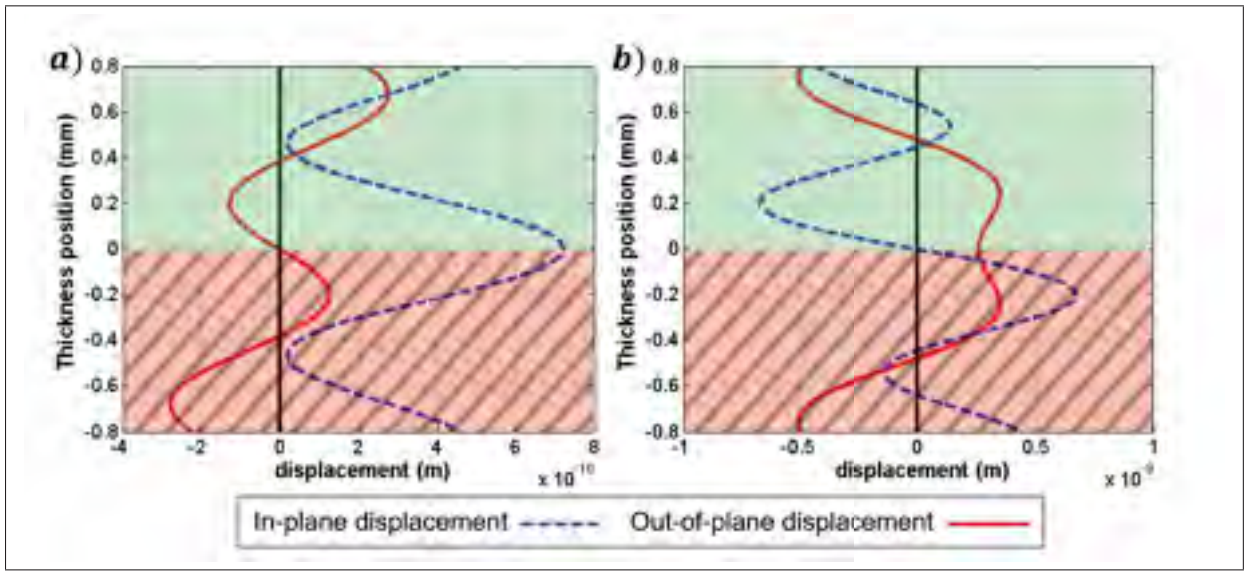

Figure 4.10 Mode shape of a) S_2 at 4 MHz and b) A_3 at 4.7 MHz for the A_3 conversion from S_2 reflection

This means that when S_2 is reflected by part through-thickness crack, of which the depth is lower than 50% of the plate thickness, the A_3 mode is reflected by the interaction between S_2 and the crack. This corresponds to the green zone in Figure 4.10. For a crack between 0% and 50% of depth, the amount of A_3 converted from S_2 increases over the crack depth as the surface of the mode reflection increases. When the crack grows to a depth higher than 50%, S_2 and A_3 differ increasingly over the crack depth, thus A_3 is less and less generated from the reflection of S_2 by the part through-thickness crack as represented by the hatching zone in Figure 4.10.. When the crack depth is higher than 50%, the S_2 mode is increasingly reflected from the crack until a 100% depth.

The same reasoning can be applied to the transmitted wave. The amount of A_3

converted from S_2 and transmitted behind the crack depends on the transmission depth, calculated as the plate thickness minus the crack depth. As the transmission depth increases from 0% to 50%, the out-of-plane shape of S_2 becomes closer to the A_3 out-of-plane shape as shown in Figure 4.10 with the hatch zones.

The green zone represents the transmission depth and the hatching zone the crack depth. Thus the amount of A_3 transmitted behind the crack increases as the transmission depth increases from 0% to 50%. For a transmission depth from 50% to 100%, the mode shapes increasingly differ and S_2 is less and less converted in A_3.

The generation of A_1 and A_2 can be explained with the same type of process as the A_3 generation. However, the depth is not sizable even with the combination of the A_1, A_2 and A_3 amplitudes, shown in Figure 4.9. The antisymmetric amplitudes did not enable the attribution of a unique value of crack depth to unique values of A_1, A_2 and A_3 amplitudes.

CONCLUSION

The finite element simulations were an important part of this thesis to simulate the crack detection with varying crack parameters. All the FE models followed the same rules concerning the ratio of number of elements per wavelength and the time increment, making them stable and accurate. These models were used to study and compare guided-wave based SHM approaches.

Two guided-wave SHM approaches were studied in this thesis. The first used the fundamental symmetric guided-wave mode S_0 to detect and monitor cracks. The second exploited the high order symmetric guided-wave modes at high frequency for the same application. It appeared that both enabled the crack monitoring using the same technique. There were, however, differences in the detection limit. The low frequency detection limit was a crack between 2 mm and 3 mm long, whereas the high frequency detection limit was below 0.1 mm.

However, this improvement comes with disadvantages, which were the challenges of the high frequency guided wave study. First, the post-processing of the signals is more complex because of the mode superposition. The modes propagating in the structure must be carefully differentiated in order to achieve the interpretation of the results with accurate data. Furthermore, implementing the proposed method with high frequency requires more transducers. The density of transducers necessary for having frequency-wavenumber representations without overlaying of modes is an increasing function of the maximum wavenumber under study. The maximum wavenumber grows with the frequency; and thus the higher the frequency of excitation, the higher the density of transducers required.

The only mode propagating in the structure with the low frequency in-plane excitation was S_0. Its directivity diagrams were then used to determine the orientation and the length effects.

In terms of high frequency excitation, the S_1 mode was the most sensitive to crack length variations; thus, it was used to determine this parameter. S_2 had the highest sensitivity to the changes of crack orientation thus, this mode was used to identify the crack orientation modulo π. Lastly, the depth was not sizable with the proposed SHM method.

Moreover, the number of transducers to achieve the monitoring of cracks in this structure has to be optimized. A priori knowledge of the stress directions in the real structure would enable the measurements to be performed on a limited number of strategic orientations, thus reducing the number of transducers required. Furthermore, by taking the maximum value possible for the space step between two consecutive measurement points, the density of transducer on the output lines would be reduced and all of the modes would appear in the frequency-wavenumber representations without overlaying.

In this thesis, only the models without cracks have been validated for both low frequency and high frequency approaches. In order to confirm the legitimacy of the finite element study achieved, the modeling of cracks has to be validated against experiments.

Ultimately, the study achieved in this thesis should be repeated on other structures, like a plate with several holes or a T-beam. The optimal methodology must be determined,f and a finite element study for damage detection and monitoring must be achieved for each case.

BIBLIOGRAPHY

Alleyne, D. and P. Cawley. 1991. "A two-dimensional Fourier transform method for the measurement of propagating multimode signals". *The Journal of the Acoustical Society of America*, vol. 89, n° 3, p. 1159–1168.

Alleyne, D. N. and P. Cawley. 1992. "The interaction of Lamb waves with defects". *IEEE Transactions on Ultrasonics, Ferroelectrics, and Frequency Control*, vol. 39, n° 3, p. 381–397.

Benmedakhene, S., M. Kenane, and M. Benzeggagh. 1999. "Initiation and growth of delamination in glass/epoxy composites subjected to static and dynamic loading by acoustic emission monitoring". *Composites Science and Technology*, vol. 59, n° 2, p. 201–208.

Cawley, P., M. Lowe, D. Alleyne, B. Pavlakovic, and P. Wilcox. 2003. "Practical long range guided wave inspection-applications to pipes and rail". *Materials evaluation*, vol. 61, n° 1, p. 66–74.

Cawley, P., F. Cegla, and A. Galvagni. 2012. "Guided waves for NDT and permanently-installed monitoring". *Insight-Non-Destructive Testing and Condition Monitoring*, vol. 54, n° 11, p. 594–601.

Chan, H., B. Masserey, and P. Fromme. 2015. "High frequency guided ultrasonic waves for hidden fatigue crack growth monitoring in multi-layer model aerospace structures". *Smart Materials and Structures*, vol. 24, n° 2.

Cheeke, J. D. N., 2012. *Fundamentals and applications of ultrasonic waves*. ed. 2nd. Boca Raton, FL : CRC Press, 480 p.

Clarke, T., P. Cawley, P. D. Wilcox, and A. J. Croxford. 2009. "Evaluation of the damage detection capability of a sparse-array guided-wave SHM system applied to a complex structure under varying thermal conditions". *IEEE Transactions on Ultrasonics, Ferroelectrics, and Frequency Control*, vol. 56, n° 12, p. 2666–2678.

Cook, R. D. et al., 2007. *Concepts and applications of finite element analysis*. ed. 4th. Hoboken, NJ : John Wiley & Sons.

Croxford, A., P. Wilcox, B. Drinkwater, and G. Konstantinidis. 2007. "Strategies for guided-wave structural health monitoring". *Proceedings of the Royal Society of London A: Mathematical, Physical and Engineering Sciences*, vol. 463, n° 2087, p. 2961–2981.

Dalton, R., P. Cawley, and M. Lowe. 2001. "Propagation of acoustic emission signals in metallic fuselage structure". *IEE Proceedings - Science, Measurement and Technology*, vol. 148, n° 4, p. 169–177.

Deraemaeker, A., E. Reynders, G. De Roeck, and J. Kullaa. 2008. "Vibration-based structural health monitoring using output-only measurements under changing environment". *Mechanical systems and signal processing*, vol. 22, n° 1, p. 34–56.

Drozdz, M., E. Skelton, R. V. Craster, and M. J. S. Lowe. 2007. "Modeling bulk and guided waves in unbounded elastic media using absorbing layers in commercial finite element packages". In *Review of Progress in Quantitative Nondestructive Evaluation*. (Portland, OR, July 30-August 4, 2006), p. 87–94. Melville, NY: AIP Publishing.

Drozdz, M. B. 2008. "Efficient finite element modelling of ultrasound waves in elastic media". PhD thesis, London, UK, Imperial College of Science Technology and Medicine, 218 p.

Farrar, C. R., S. W. Doebling, and D. A. Nix. 2001. "Vibration-based structural damage identification". *Philosophical Transactions of the Royal Society of London A: Mathematical, Physical and Engineering Sciences*, vol. 359, n° 1778, p. 131–149.

Fromme, P., P. Wilcox, M. J. Lowe, and P. Cawley. 2006. "On the development and testing of a guided ultrasonic wave array for structural integrity monitoring". *IEEE Transactions on Ultrasonics, Ferroelectrics, and Frequency Control*, vol. 53, n° 4, p. 777–785.

Galvagni, A. and P. Cawley. 2014. "Reliable Identification of Damage Growth Using Guided Wave SHM Systems". In *EWSHM-7th European Workshop on Structural Health Monitoring*. (Nantes, FR, 8-11 July, 2014). Rocquencourt, FR: Inria.

Ghosh, T., T. Kundu, and P. Karpur. 1998. "Efficient use of Lamb modes for detecting defects in large plates". *Ultrasonics*, vol. 36, n° 7, p. 791–801.

Giurgiutiu, V., 2014. *Structural health monitoring with piezoelectric wafer active sensors*. ed. 2nd. Oxford, UK : Academic Press, 1012 p.

Glisic, B. and D. Inaudi, 2007. *Fibre optic methods for structural health monitoring*. Chichester, UK : John Wiley & Sons, 276 p.

Graff, K. F., 1991. *Wave motion in elastic solids*. New York, NY : Dover Publications, 688 p.

Huthwaite, P. 2014. "Accelerated finite element elastodynamic simulations using the GPU". *Journal of Computational Physics*, vol. 257, Part A, p. 687 - 707.

Lamb, H. 1917. "On waves in an elastic plate". *Proceedings of the Royal Society of London A: Mathematical, Physical and Engineering Sciences*, vol. 93, n° 648, p. 114–128.

Lowe, M. J., D. N. Alleyne, and P. Cawley. 1998. "Defect detection in pipes using guided waves". *Ultrasonics*, vol. 36, n° 1, p. 147–154.

Masserey, B. and P. Fromme. 2013. "Fatigue crack growth monitoring using high-frequency guided waves". *Structural Health Monitoring*, vol. 12, n° 5-6, p. 484–493.

Mazille, H., R. Rothea, and C. Tronel. 1995. "An acoustic emission technique for monitoring pitting corrosion of austenitic stainless steels". *Corrosion Science*, vol. 37, n° 9, p. 1365–1375.

Mckeon, P., S. Yaacoubi, N. Declercq, and S. Ramadan. 2012. "Issues concerning using mode conversion of guided waves to size defects in plates". In *Acoustics 2012*. (Nantes, FR, April 23-27, 2012). Société Française d'Acoustique.

Park, G. and D. J. Inman. 2005. "Impedance-based structural health monitoring". *Damage prognosis - For aerospace, civil and mechanical systems*, p. 275–292.

Pavlakovic, B., M. Lowe, D. Alleyne, and P. Cawley. 1997. "Disperse: A General Purpose Program for Creating Dispersion Curves". In *Review of Progress in Quantitative Nondestructive Evaluation*. (Brunswick, ME, Jul. 28-Aug. 2, 1996), p. 185-192. New York, NY: Plenum Press.

Raghavan, A. and C. E. S. Cesnik. 2007. "Review of guided-wave structural health monitoring". *Shock and Vibration Digest*, vol. 39, n° 2, p. 91–116.

Rajagopal, P., M. Drozdz, E. A. Skelton, M. J. S. Lowe, and R. V. Craster. 2012. "On the use of absorbing layers to simulate the propagation of elastic waves in unbounded isotropic media using commercially available finite element packages". *NDT & E International*, vol. 51, p. 30–40.

Rayleigh, L. 1888. "On the free vibrations of an infinite plate of homogeneous isotropic elastic matter". *Proceedings of the London Mathematical Society*, vol. 20, n° 357, p. 225–237.

Roberts, T. M. and M. Talebzadeh. 2003. "Acoustic emission monitoring of fatigue crack propagation". *Journal of Constructional Steel Research*, vol. 59, n° 6, p. 695–712.

Rose, J. L., 1999. *Ultrasonic waves in solid media*. New York, NY : Cambridge University Press, 472 p.

Shull, P. J., 2002. *Nondestructive evaluation: theory, techniques, and applications*. New York, NY : CRC Press, 876 p.

Simulia, D. 2013. "Abaqus 6.13 User's Manual". *Dassault Systems, Providence, RI*.

Solie, L. and B. Auld. 1973. "Elastic waves in free anisotropic plates". *The Journal of the Acoustical Society of America*, vol. 54, n° 1, p. 50–65.

Staszewski, W., B. Lee, L. Mallet, and F. Scarpa. 2004. "Structural health monitoring using scanning laser vibrometry: I. Lamb wave sensing". *Smart Materials and Structures*, vol. 13, n° 2, p. 251.

Staszewski, W., B. Lee, and R. Traynor. 2007. "Fatigue crack detection in metallic structures with Lamb waves and 3D laser vibrometry". *Measurement Science and Technology*, vol. 18, n° 3, p. 727–739.

Tua, P., S. Quek, and Q. Wang. 2004. "Detection of cracks in plates using piezo-actuated Lamb waves". *Smart Materials and Structures*, vol. 13, n° 4, p. 643.

Wilcox, P., M. Evans, B. Pavlakovic, D. Alleyne, K. Vine, P. Cawley, and M. Lowe. 2003. "Guided wave testing of rail". *Insight-Non-Destructive Testing and Condition Monitoring*, vol. 45, n° 6, p. 413–420.

Wilcox, P., M. Lowe, and P. Cawley. 2001. "A signal processing technique to remove the effect of dispersion from guided wave signals". In *Review of Progress in Quantitative Nondestructive Evaluation.* (Ames, IA, July 16-20, 2000), p. 555–562. Melville, NY: AIP Publishing.